INERTIAL MIGRATION OF DEFORMABLE CAPSULES AND DROPLETS IN OSCILLATORY AND PULSATING MICROCHANNEL FLOWS

by

Ali Lafzi

A Dissertation

Submitted to the Faculty of Purdue University

In Partial Fulfillment of the Requirements for the degree of

Doctor of Philosophy

School of Agricultural and Biological Engineering

West Lafayette, Indiana

May 2022

THE PURDUE UNIVERSITY GRADUATE SCHOOL
STATEMENT OF COMMITTEE APPROVAL

Dr. Sadegh Dabiri, Chair

Department of Agricultural and Biological Engineering and School of Mechanical Engineering

Dr. Mohit Verma

Department of Agricultural and Biological Engineering

Dr. Arezoo M. Ardekani

School of Mechanical Engineering

Dr. Steven T. Wereley

School of Mechanical Engineering

Approved by:

Dr. Nathan S. Mosier

ACKNOWLEDGMENTS

I would like to express my sincere gratitude to my Ph.D. advisor, Prof. Sadegh Dabiri, for providing me with the chance to conduct my research and study at Purdue University. His knowledge, patience, and expertise made it possible to overcome the challenges and helped me think critically and creatively. Furthermore, I would appreciate my committee members Prof. Arezoo Ardekani, Prof. Steve Wereley, and Prof. Mohit Verma for their insightful comments and encouragement.

I would also like to acknowledge Rice, Brown, and Bell High-Performance Computing Clusters for providing the necessary tools for my numerical simulations. I want to thank all the professors at Purdue whose courses I have been a part of, who have helped expand my knowledge and skills in different areas.

I express my sincere gratitude to the staff at the Department of Agricultural and Biological Engineering, especially Nicole Zimmerman, the Graduate Program Administrator, for facilitating my transition to the Purdue graduate school and for all her kind support during difficult and complicated situations I faced. I should also thank Pamela Hancock at the business office for her guidance through all the financial logistics and David Wilson for his assistance with the lab demonstrations I had when I was a teaching assistant for the undergraduate Thermodynamics class.

I am grateful to all my colleagues, Amir Hossein, Calvin, Pramod, Maathangi, Pranav, Tyler, and Ilyas for their constant constructive feedback during meetings and discussions. I would also like to acknowledge all my friends at Purdue for their help and moral support.

Last but not least, I would like to thank my dear parents, Ardeshir and Fariba, for their unconditional support and consistent encouragement throughout my entire life and for giving me the strength to reach for the stars and chase my dreams. Also, I wholeheartedly thank my fiancee, Niyousha, who stood by me through all my travails and the ups and downs of my life in the past 3 years. Without her encouragement, patience, love, and continuous support, this achievement would not have been possible.

TABLE OF CONTENTS

LIST OF TABLES

LIST OF FIGURES

ABSTRACT

Studying the motion of cells and investigating their migration patterns in inertial microchannels have been of great interest among researchers because of their numerous biological applications such as sorting, separating, and filtering them. A great drawback in conventional microfluidics is the inability to focus extremely small biological particles and pathogens in the order of sub-micron and nanometers due to the requirement of designing an impractically elongated microchannel, which could be in the order of a few meters in extreme cases. This restriction is because of the inverse correlation between the cube of the particle size and the theoretically required channel length. Exploiting an oscillatory flow is one solution to this issue where the total distance that the particle needs to travel to focus is virtually extended beyond the physical length of the device. Due to the present symmetry in such flow, the directions of the lift forces acting on the particle remain the same, making the particle focusing feasible.

Here, we present results of simulation of such oscillatory flows of a single capsule in a rectangular microchannel containing a Newtonian fluid. A 3D front-tracking method has been implemented to numerically study the dynamics of the capsule in the channel of interest. Several cases have been simulated to quantify the influence of the parameters involved in this problem such as the channel flow rate, capsule deformability, frequency of oscillation, and the type of applied mechanism for inducing flow oscillations. In all cases, the capsule blockage ratio and the initial location are the same, and it is tracked until it reaches its equilibrium position. The capability to focus the capsule in a short microchannel with oscillatory flow has been observed for capsule deformabilities and mechanisms to induce the oscillations used in our study. Nevertheless, there is a limit to the channel flow rate beyond which, there is no single focal point for the capsule. Another advantage of having an oscillatory microchannel flow is the ability to control the capsule focal point by changing the oscillation frequency according to the cases presented in the current study. The capsule focusing point also depends on its deformability, flow rate, and the form of the imposed periodic pressure gradient; more deformable capsules with lower maximum velocity focus closer to the channel center. Also, the difference between the capsule equilibrium point in steady and oscillatory

flows is affected by the capsule stiffness and the device flow rate. Furthermore, increasing the oscillation frequency, capsule rigidity, and system flow rate shorten the essential device length.

Although the oscillation frequency can provide us with new particle equilibrium positions, especially ones between the channel center and wall that can be very beneficial for separation purposes, it has the shortcoming of having a zero net throughput. To address this restriction, a steady component has been added to the formerly defined oscillatory flow to make it pulsating. Furthermore, this type of flow adds more new equilibrium points because it behaves similarly to a pure oscillatory flow with an equivalent frequency in that regard. They also enable the presence of droplets at high Ca or Re that could break up in the steady or a very low-frequency regime. Therefore, we perform new numerical simulations of a deformable droplet suspended in steady, oscillatory, and pulsating microchannel flows. We have observed fluctuations in the trajectory of the drop and have shown that the amplitude of these oscillations, the average of the oscillatory deformation, and the average migration velocity decrease by increasing the frequency. The dependence of the drop focal point on the shape of the velocity profile has been investigated as well. It has been explored that this equilibrium position moves towards the wall in a plug-like profile, which is the case at very high frequencies. Moreover, due to the expensive cost of these simulations, a recursive version of the Multi Fidelity Gaussian processes (MFGP) has been used to replace the numerous high-fidelity (or fine-grid) simulations that cannot be afforded numerically. The MFGP algorithm is used to predict the equilibrium distance of the drop from the channel center for a wide range of the input parameters, namely Ca and frequency, at a constant Re. It performs exceptionally well by having an average R^2 score of 0.986 on 500 random test sets.

The presence of lift forces is the main factor that defines the dynamics of the drop in the microchannel. The last part of this work will be dedicated to extracting the active lift force profiles and identify their relationships with the parameters involved to shed light on the underlying physics. This will be based on a novel methodology that solely depends on the drop trajectory. Assuming a constant Re, we then compare steady lift forces at different Ca numbers and oscillatory ones at the same constant Ca. We will then define analytical

equations for the obtained lift profiles using non-linear regression and predict their key coefficients over a continuous range of inputs using MFGP.

1. INTRODUCTION

Manipulation of particles suspended in laminar flows in microchannels is commonly used in a variety of applications in bioparticle separation and filtration systems [1]. Depending on flow physics, the geometry of channel, and particles characteristics such as shape, size, and deformability, suspended particles focus in different regions of the channel, which can be used for sorting, isolating, or separating them for diagnostic and biological purposes [2]–[5]. Diagnosing circulating tumor cells (CTCs) has always been of great interest, and due to heterogeneity of them, molecular assays and microfluidic technologies are required for cancer type-specific isolation [6]. Similarly, micro-scale vortices and inertial focusing were combined to extract CTCs from blood samples [7]. Another important advantage of these systems is being non-invasive; molecular cytogenetic techniques were used to identify fetal cells from maternal cells [8].

One of the important shortcomings of current procedures, however, is their low flow throughput. Therefore, there have been many studies to address this issue in numerous applications. *Di Carlo et al.* [9] used an asymmetrically curved channel to enhance the volume throughput and filter deformable particles with varying sizes. Spiral microfluidic devices, having greater throughput compared to that of the existing microfluidic systems, have been introduced for cell separation and isolation [10], [11]. Removal of leukocytes (white blood cells) from the whole blood can be done with a continuous flow diffusive filter; isolation of plasma is also possible with simple modifications to the device [12]. *Gossett et al.* [13] demonstrated an automated technology to assay cell deformability at very high throughputs. *Ozkumur et al.* [14] have described a technology that can sort rare CTCs from the whole blood at a very high throughput of 10^7 cells/s. Repetitive inertial focusing combined with micro-siphoning resulted in a microfluidic bioparticle concentrator [15]. Stacked and cascaded inertial focusing strategies have been developed to achieve high throughput and concentrate desired particle size [16]. Label and sheath-free inertial microfluidics were exploited for cell differentiation and blood fractionation with a high throughput [17], [18].

In addition to inertial microfluidics, people have utilized electrical characteristics in the system. For instance, *Gascoyne et al.* [19] have used dielectrophoretic field-flow-fractionation

as a microfluidic approach to malaria detection. *Vahey and Voldman* [20] implemented a continuous-flow and label-free microfluidic filter capable of separating cells based on their electrical polarizability. Biochemical markers have also been used for cell sorting. *Miltenyi et al.* [21] reported a simple magnetic system as a complement to flow cytometry. A microfabricated membrane was designed to perform in situ cell lysis with a very high efficiency [22]. These methods are, however, costly and complex and hence, less used in clinical applications compared to label-free approaches.

Although inertial microfluidics has a broad range of applications, most of the common practices are limited to control particles in the order of few microns in radius or larger (red blood cells, for instance) [23]. This restriction is because small particles need to travel a very long distance to focus since the inertial lift force decreases for smaller particles. The theoretical length at which point particles travel to focus is inversely proportional to the cube of their radius. This can be shown by adopting a similar method *Di Carlo et al.* [24] applied to finite particles. Hence for the case of nanoparticles, this traveling distance can reach up to the order of meters, which makes it practically impossible for design purposes [23]. Nevertheless, it is vital to study small bioparticles, such as bacteria and fungi, due to their effective role in diagnosis. For instance, it is crucial to track microvesicles released by Glioblastoma tumor cells as they are beneficial in cancer patient care [25], [26]. There are only a few examples of working with smaller pathogens, such as separating pathogenic bacteria cells from diluted blood and detecting malaria parasites from blood [27], [28]. Moreover, a microchannel with multiple branches was shown to enable separation of smaller particles compared to that obtained with conventional pinched flow fractionation (PFF), but the size of separated particles is still not as small as desired [29]. Therefore, it is momentous to develop methods that can be applied to study small bioparticles and pathogens in a practical manner.

In addition, the dynamics of capsules, droplets, and particles in oscillatory microchannels has become of interest to many researchers recently; A simple equation containing only the Taylor deformation parameter and viscosity ratio has been proposed to estimate the threshold frequency for the capsule deformation behavior in an oscillatory shear flow in the Stokes flow regime [30]. *Bryngelson and Freund* [31] have done a non-modal and time-global

Floquet stability analysis for a spherical capsule subject to a large-amplitude oscillatory extensional flow and found that all flow strengths (or a corresponding Weissenberg number) and oscillation frequencies are asymptotically stable despite experiencing some transient instabilities. The dynamics of formation and stability of particle pairs in an oscillatory flow in a microchannel has been investigated experimentally, and a linear correlation between the particle-particle interactions and flow velocity has been determined [32]. *Chaudhury et al.* [33] have observed a complicated trajectory of the droplet in the lateral direction suspended in an oscillatory flow as opposed to the smooth cross-stream migration under steady flow conditions. *Pawlowska et al.* [34] have reported the use of hydrogel nanofilaments as an appropriate substitute for the long and deformable macromolecules and studied their dynamics in an oscillatory microchannel flow. They have shown that the final position of these particles fluctuates around the flow axis [35]. *Sarkar and Schowalter* [36] have investigated the dynamics of a viscoelastic drop in steady and oscillating extensional flows and have shown that although their deformation behaviors are naturally dissimilar, their maximum values are close in the long-time limit. *Zhang et al.* [37] have found that the effect of capsule membrane viscosity is more significant in the oscillatory shear flow compared to that of the steady one, and the deformation of capsule is influenced by both viscosity and elasticity and exhibits two modes. *Lu et al.* [38] have performed a numerical and experimental study on an ultrasonic oscillatory airwater two-phase flow in a microchannel. They have observed highly unsteady behavior as the water and air interact with each other during the vibration cycles, which is drastically different from the steady flow in such microchannels.

In chapter 2, we implement the idea of oscillatory inertial microfluidics in microchannels, expressed by *Mutlu et al.* [23]. The advantage of this method is that by changing the direction of the flow at a certain frequency, the virtual length at which the particle can travel is extended beyond the physical length of the channel. Due to the symmetrical flow conditions, the directions of forces acting on the particle in the wall-normal direction remain the same. Therefore, small particles corresponding to small values of particle Reynolds number ($Re_p < 0.1$) can reach their focal position in a short physical length of the device, which was otherwise unfeasible. Furthermore, it will be shown that the frequency of flow oscillation influences the equilibrium position of capsules in the channel. This parameter

can be used as an extra tool for direct control over the dynamics of capsules. Besides, the oscillation frequency as the new extra parameter does not have the disadvantage of adversely affecting the biological properties of cells like most of the active methods [39].

In chapter 3, we investigate different aspects of the droplet migration in oscillatory and pulsating microchannel flows numerically and compare them with those in the steady ones. The main challenge of performing this numerical work is using a sufficient grid resolution to resolve the underlying physics more accurately. Since the background flow is unsteady, the mesh has to be fine enough to capture the velocity gradients and lift forces acting on the drop correctly. Consequently, the transient dynamics of the drop and its final equilibrium position, which is the main goal of the presented study, are all affected by this choice. Therefore, after carrying out the mesh dependence study, a very fine grid has been selected to enable getting the realistic results we are interested in. However, running simulations with these grids can take a few months in some cases. Hence, it is impossible to get all the data in the wide range of input parameters we are looking for by just running all these simulations. An alternative approach is to produce some new data using a coarser grid resolution and implement the Multi Fidelity Gaussian processes (MFGP) algorithm to predict the outputs of the finer mesh. *Perdikaris et al.* [40] have proposed a probabilistic framework and a recursive version of MFGP. This method has been tested in several benchmark problems involving both synthetic and real multi-fidelity datasets such as the one employed by *Babaee et al.* [41]. The implementation of the recursive MFGP and the obtained results in this study are elaborated in the following sections.

The presence of lift forces acting on bioparticles is the chief reason for observing the underlying physical phenomena in microfluidic systems [24], [42]–[45]. The importance of these forces has motivated many researchers to analyze or measure them within the microchannel. *Di Carlo et al.* have derived the inertial lift on particles and studied the effects of channel Reynolds number and particle size on it; they have shown that by increasing Reynolds, the magnitude of lift coefficient decreases near the wall and increases near the channel center [46]. Also, the particle equilibrium positions shift toward the center as its size increases and its rotational motion is not a key component of the inertial lift. Using lift force profiles, *Prohm and Stark* have investigated and categorized the particle focusing points and demonstrated

that the stable fix points lie on either the diagonal or main axes of the channel cross-section [47]. *Su et al.* have proposed a fast numerical algorithm combined with machine learning techniques to predict the inertial lift distribution acting on solid particles over a wide range of operating parameters in straight microchannels with three types of geometries by specifying the cross-sectional shape, Reynolds number, and particle size [48].

Furthermore, there have been attempts to derive analytical relationships for the observed behaviors. A simple formula using data fitting and least square was obtained to investigate the relationship between the lift and particle size and Reynolds number; according to the proposed criterion, particle focusing does not occur for too small particles or too low Reynolds numbers [49]. *Asmolov et al.* illustrated that the velocity of finite-size particles near the channel wall is different from that in the undisturbed flow and then reported a generalized expression for the lift force at $\mathrm{Re} \leq 20$ [50]. Another study has proposed a generalized formula for the inertial lift acting on a sphere that consists of 4 terms: wall-induced lift, shear-gradient-induced lift, slip-shear lift, and correction of the shear-gradient lift; the authors have further confirmed that wall and shear-gradient are the main features of the lift [51]. Moreover, there are examples of works concentrating on the effect of particle shape. For instance, *Zastawny et al.* presented the great influence of shape both by changing the experienced values of forces and torques and modifying the Reynolds at which the transition to unsteady flow happens [52]. Further extension on previous theories and analytical works resulted in an analytical expression capturing the weak, inertial lift on an arbitrarily-shaped particle moving near a wall [53].

Most of the studies on lift forces in the microchannels have focused on solid particles or non-deformable objects and have analyzed the effect of parameters such as channel Reynolds, particle size, etc. Therefore, there are very few examples presenting the whole lift force profiles acting on deformable particles such as droplets and bubbles and studying the effect of their corresponding parameters like Capillary number on the force values. For example, *Chen et. al* have extensively studied the inertial migration of a deformable droplet in a rectangular microchannel, but their presented lift force profile only considers one value for particle Weber number (a measure for particle deformability) [54]. *Rivero Rodriguez and Scheid* have divided the underlying physics into different regimes. In the pure inertial regime,

they have plotted the inertial lift on a rigid bubble at different Reynolds numbers, and in the pure Capillary regime where the inertial effects are absent, a lift profile is presented for different Capillary numbers [55]. However, their work lacks a similar profile visualizing the total lift force in the most general nonlinear inertial-capillary regime.

The obtained lift force profiles are mainly the result of either some experimental measurements [46], [56], [57] or applying a feedback control in the numerical code to fix the position of particle [58], capsule [59], or drop [54]. Nevertheless, in chapter 4, we present a method for lift force calculation at different Capillary numbers that solely depends on the trajectory of the drop. In addition, due to the importance of exploiting oscillatory flows in microchannels as previously mentioned, we will expand our lift force analysis to include both steady and oscillatory regimes at various Capillary numbers, where the latter is completely missing in the literature. We will then try to fit analytical expressions to the obtained lift profiles for different cases and present a scheme to predict this expression over a continuous range of input parameters.

2. INERTIAL MIGRATION OF A DEFORMABLE CAPSULE IN AN OSCILLATORY FLOW IN A MICROCHANNEL

2.1 Summary

Dynamics of a deformable capsule in an oscillatory flow of a Newtonian fluid in a microchannel has been studied numerically. The effects of oscillation frequency, capsule deformability, and channel flow rate have been explored by simulating the capsule within a microchannel. In addition, the simulation captures the effect of the type of imposed pressure oscillations on the migration pattern of the capsule. An oscillatory channel flow enables the focusing of extremely small biological particles by eliminating the need to design impractically long channels. The presented results show that the equilibrium position of the capsule changes not only by the addition of an oscillatory component to the pressure gradient, but it also is influenced by the capsule deformability and channel flow rate. Furthermore, it has been shown that the amplitude of oscillation of capsules decreases as the channel flow rate and the rigidity of the capsule increases.

2.2 Methodology

A single deformable capsule has been placed in a laminar flow of an incompressible Newtonian fluid in a microchannel with a square cross-section. A schematic of the configuration is illustrated in Fig. 3.1(a). The density and viscosity of the inner Newtonian fluid inside the capsule are the same as those of the outer one. The front-tracking method [60] is used to track the position of the interface. The front consists of Lagrangian grid points connected by triangular elements (Fig. 3.1(b)). In this method, the main governing equations (equations (2.1) and (2.2)) are solved for both fluids inside and outside of the capsule on a fixed Eulerian grid. The local velocity of the fluid is used to move the Lagrangian points on the capsule membrane under the assumption of no-slip condition on the capsule membrane. The governing equations to be solved in the entire computational domain are the following:

$$\nabla \cdot \mathbf{u} = 0, \tag{2.1}$$

$$\frac{\partial(\rho\mathbf{u})}{\partial t} + \nabla\cdot(\rho\mathbf{u}\mathbf{u}) = -\nabla P + \nabla\cdot[\mu(\nabla\mathbf{u} + \nabla\mathbf{u}^T)] + \mathbf{F}, \tag{2.2}$$

where ρ and μ are the density and viscosity of both fluids respectively, P represents the pressure, $\mathbf{u}$ is the velocity vector, t is the time, and $\mathbf{F}(\boldsymbol{x},t) = \int_{\partial B}\boldsymbol{f}(\boldsymbol{x}_\mathrm{i},t)\delta(\boldsymbol{x}\text{-}\boldsymbol{x}_\mathrm{i})dV$, which is the smoothed representation of the membrane elastic force. This is shown by placing a Dirac delta function within the integral, where $\boldsymbol{x}$ is an arbitrary location in the whole computational domain and $\boldsymbol{x}_\mathrm{i}$ is such position on the capsule membrane. The given delta function is defined as:

$$\delta(X) = \tilde{D}(x)\tilde{D}(y)\tilde{D}(z), \tag{2.3}$$

$$\tilde{D}(x) = \begin{cases} \frac{1}{4\Delta}(1+\cos(\frac{\pi}{2\Delta}(x))) & |x| \le 2\Delta, \\ 0 & \text{otherwise}, \end{cases} \tag{2.4}$$

where Δ is the constant Eulerian grid size. The capsule membrane is assumed to be an infinitely thin sheet of elastic material. Using the Skalak model [61], we assign the following strain energy function to the capsule membrane:

$$W = \frac{E_s}{12}((\epsilon_1^2+\epsilon_2^2-2)^2 + 2(\epsilon_1^2+\epsilon_2^2-2) - 2(\epsilon_1^2\epsilon_2^2-1)) + \frac{E_a}{12}(\epsilon_1^2\epsilon_2^2-1)^2, \tag{2.5}$$

Here, ϵ_1 and ϵ_2 are the principal strains, and E_s and E_a represent the shear and area dilatation moduli, respectively. We consider $\frac{E_a}{E_s} = 2$ according to *Kruger et al.* [62]. Bending resistance has not been taken into account as its effect is negligible compared to that of the shear modulus [63]. A finite element method [64] is used to calculate the forcing term $\boldsymbol{f}$. The membrane surface is discretized with a large number of triangular elements so that they remain approximately flat in case of undergoing large deformations. The resultant elastic force ($\boldsymbol{f}(\boldsymbol{x}_\mathrm{i},t)$) acting on the membrane is found using the principle of virtual work. The validation of this model against previously published results and a more detailed explanation of this whole methodology can be found in *Raffiee et al.* [65].

Two forms of oscillatory pressure gradients have been applied along the channel (x direction) to change the direction of the flow symmetrically: a) A cosine wave with a constant

amplitude (in the form of $P_0 cos(\omega t)$) b) A square wave with the same average and ω as that of the cosine wave; so P_0 is different. The periodic boundary condition is applied in the x direction, and the no-slip condition is applied on the walls in the y and z directions. W, U_c (maximum velocity of the steady flow), and $\frac{W}{U_c}$ are used to nondimensionalize all lengths, velocities, and time, respectively. In other words, $x^* = \frac{x}{W}$, $u^* = \frac{u}{U_c}$, $t^* = \frac{t}{\frac{W}{U_c}}$, $P^* = \frac{P}{\mu \frac{U_c}{W}}$, $T^* = \frac{T}{\frac{W}{U_c}}$ (where T is the period), and $\omega^* = \frac{2\pi}{T^*}$. Two dimensionless parameters describe the motion of the capsule: (i) Reynolds number, $Re = \frac{\rho U_c 2W}{\mu}$, expressing the ratio between inertial forces to viscous ones (ii) Laplace number, $La = \frac{2aE_s\rho}{\mu^2}$, which denotes the deformability of the capsule, where low La corresponds to highly deformable capsules, and high La represents more rigid particles. The blockage ratio of the capsule ($\frac{a}{W}$) is constant and equal to 0.3. The capsule is assumed to have a spherical initial shape and is released at $\frac{y}{W} = 0.55$ and $\frac{z}{W} = 1.07$. The initial location of the capsule is arbitrary because it only affects the initial, transient stage of the capsule migration and does not influence its long-term behavior and focusing point [66]–[69]. The axes of symmetry are also avoided for the initial location of the capsule. The time step of the simulation is restricted by the Courant-Friedrichs-Lewy (CFL) number, which is set to 0.9. An Eulerian grid of $200 \times 115 \times 115$ in the x, y, and z directions, respectively, and 48672 triangular elements for the discretization of the capsule surface are used in most of the simulations. For the cases with $Re > 10$, we use $256 \times 152 \times 152$ Eulerian grid points and 80000 Lagrangian elements.

2.3 Results and discussion

2.3.1 Sinusoidal oscillatory flow

We study the effects of inertia, deformability, and pressure oscillations frequency on the migration of the capsule by adjusting Re, La, and ω^*. Re ranges between 5 and 37.8, La ranges between 1 and 500, and ω^* values are chosen such that for a channel with a square cross-section of $100\mu m$ and water as the working fluid at room temperature, the frequency values range between 2Hz and 200Hz, which is mostly reported in the literature [70]. For each case, the capsule is placed at the same initial location in the channel and is tracked until it reaches its focal position. This equilibrium position is a result of the competition

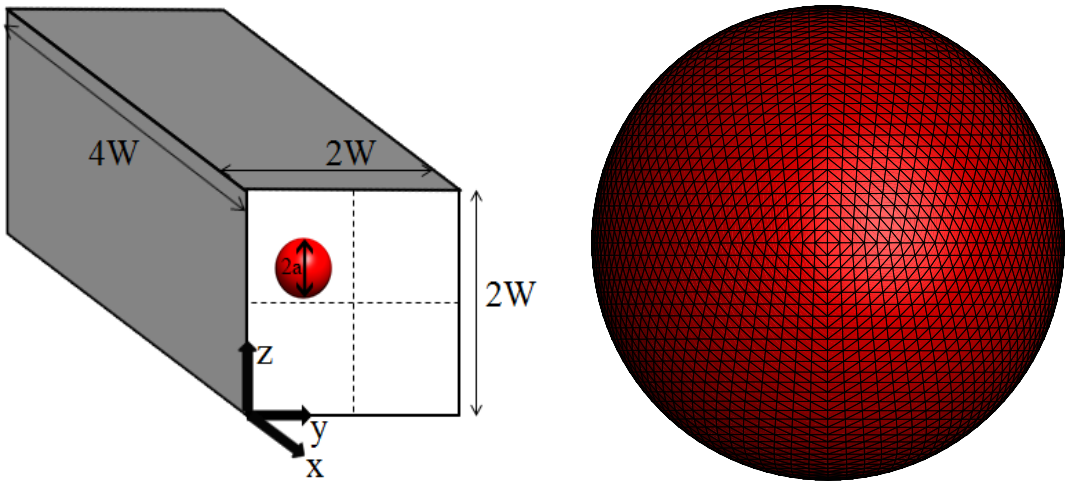

(a) (b)

Figure 2.1. (a) Schematic of the problem setup and (b) An example of the capsule discretization

between the forces acting on the capsule, namely the wall effect and the capsule deformation-induced lift forces, both acting towards the channel center, and the shear gradient force acting towards the wall [71], [72]. Magnus and Saffman lift forces are often very small and negligible compared to the other mentioned components [72]. The role of the boundary wall is to generally retard the particle motion. When the particle moves parallel to the wall, it experiences a transverse lift force that repels it away from the wall [72]. The existing curvature of the parabolic fluid velocity profile makes the magnitude of the relative velocity of the fluid to that of the particle on the wall side much higher than the channel center side. This dissymmetry causes a low pressure on the wall side resulting in a shear gradient lift force that pushes the particle towards the closer wall from the channel center [72]. To the best of our knowledge, there is no quantitative expression for the shear gradient force in the literature to date. Following the analytical results of *Chan and Leal* [73], the deformability-induced lift force for droplets or bubbles that have a distance higher than their diameter from the wall, which is the case in our simulations, is given by [74]:

$$F_{L,deformation} = -75.4 Ca_p \mu V_{avg} a (\frac{a}{W})^2 \frac{d}{W}, \tag{2.6}$$

$$Ca_p = \frac{\mu V_{avg}}{\gamma} \frac{a}{W}, \tag{2.7}$$

Where Ca_p is the particle capillary number, V_{avg} is the average velocity of the carrier fluid across the channel, d is the distance of the particle from the channel center, and γ is the surface tension at the interface. Here, $f(\lambda)$ in the original equation, (where λ is the viscosity ratio between the inner and outer fluids), is replaced with its value of -75.4 evaluated at $\lambda = 1$. The negative sign indicates that this force acts towards the center of the channel.

Fig. 2.2 depicts the effect of frequency, capsule deformability, and channel flow rate on the capsule dynamics. In these sub-figures, d^* is the dimensionless distance of the capsule from the channel center. Fig. 2.2(a) illustrates this distance versus the location of the capsule along the channel. It shows that the capsule has to travel a very long distance along the flow direction in the steady flow to reach its equilibrium position. On the other hand, increasing the frequency lowers the amplitude of capsule motion due to the frequent change in the flow direction, which means that the capsule travels a shorter distance to focus; this implies that by increasing the frequency of the pressure gradient wave, the necessary length of the microfluidic channel can be decreased significantly. However, increasing the frequency steadily has its own limitations, as it is challenging to create very high frequencies in practice [75]. In particular, the case of $\omega^* = 0.1$ is plotted by dots at equal time intervals. The varying distance between its consecutive points is due to the sinusoidal pressure gradient.

Fig. 2.2(b) shows the time evolution of the distance of the capsule from the center of the channel for several cases. The most important feature of this figure is the change in the focal point of the capsule due to the change in the frequency of oscillation. This is because the wall effect and shear gradient induced lift forces directly depend on the flow velocity, which has a different quantitative profile for different frequency values. This, in turn, changes the lateral location of the capsule leading to changes in the deformation-induced lift force [72].

Fig. 2.2(c) shows the equilibrium location of all the cases in this study. At $Re = 10$ and all the La numbers, there is an intermediate value of frequency at which the capsule focuses closer to the channel center compared to the steady and other oscillatory cases. This frequency depends on both the capsule deformability and channel flow rate. Since V_{avg} is a

function of time in the oscillatory flows, an appropriate approach to interpret it is to refer to its average in a portion of the corresponding periodic cycle when the flow is in a single direction (half a period). For the higher frequency at the same amplitude of the pressure gradient, the absolute value of the average of V_{avg} in each half a periodic cycle is lower. This is confirmed by comparing the corresponding flow rates in the channel. This further implies that the maximum of U_c in each cycle decreases by increasing the frequency. Therefore, at higher frequencies, both deformation and shear gradient forces are lower on average; this is because of equation (2.6) and the resultant lower difference between the relative velocities on the wall and channel sides, respectively. From Fig. 2.2(c), we can conclude that by increasing the frequency to a particular value, the decrease in the shear gradient force is more than that of the deformation force, making the latter the dominant one. Above this critical frequency, the decrease in the deformation force is more, which makes the shear gradient lift the overcoming force. At $Re = 25$ and $Re = 37.8$, however, increasing the frequency leads to a focusing point closer to the center. This means that the average deformation force always overcomes the average shear gradient lift at higher Reynolds. The wall-induced lift force for all the studied cases here is negligible as the capsule paths are far from the wall. [72]

It is also notable from Fig. 2.2(c) that at the fixed $Re = 10$, there is an intermediate value of La number ($La = 50$ in the figure) for which the differences between the capsule focal points in the steady and oscillatory flows at the depicted frequencies are higher than those for the other capsule deformabilities. This is because by changing the frequency, the capsule generally begins to travel a different trajectory due to the change in the flow motion pattern and values of the shear gradient lift force. Since the deformation lift force also depends on the capsule location and shear, its magnitude will also be different by changing the frequency. This means that the change in the values of both lift forces contributes to different focal points at different frequencies. However, when La is very high ($La = 500$ and $La = 250$ for instance), the capsule cannot deform much resulting in close values of the deformation-induced force. This behavior can also be observed in equation (2.6) as the Ca_p is a small value due to the consequence of the $Ca_p = \frac{Re_p}{La}$ relationship [59]. Therefore, the difference between the focal points at different frequencies only comes from different magnitudes of the shear gradient force. On the other hand, at $Re = 10$ and $La = 10$, we

can observe that for all the studied frequencies, the capsule focuses close to the center. This is because La is very low for this case, and so the deformation force dominates the shear gradient force repelling the capsule towards the center regardless of the flow motion pattern. Thus, the difference between the focal points at different frequencies in this case only comes from different magnitudes of the deformation force.

Furthermore, increasing Re increases the distance between the focal points of the capsule in the flows with the frequencies depicted in Fig. 2.2(c) (including the steady flows) at the same La. This is due to the higher change in the corresponding shear gradient and deformation lift forces as a consequence of the higher difference between the absolute values of the average of V_{avg} in each half a periodic cycle at different frequencies. This is also confirmed by comparing the differences among the average of flow rates in the steady and oscillatory flows by keeping ω^* and La fixed and changing Re only. Another possible explanation for this phenomenon could be the effect of the Re_p term in the inertial lift force equation reported in *Di Carlo et al.* [46] ($F_{L,inertial} = -10Re_p\mu V_{avg}a\frac{d}{W}$) although the restricted criteria of $\frac{d}{W} < 0.2$ for validity of this equation does not apply to all the cases in our work.

Due to the square shape of the channel cross-section, the inherent symmetry is reduced compared to the *Segre and Silberberg* effect [76], which is the appearance of colloidal particles on the circular annulus. Therefore, there is a set of discrete equilibrium points on the main axes and diagonal of the cross-section instead [47]. It has been reported in the literature that larger particles migrate towards the diagonal, where they are further away from the walls, while smaller particles migrate towards the main axes [59]. Fig. 2.2(d) shows the lateral migration of the capsule on the channel cross-section, where the solid black line is the diagonal. While most of the cases including all the steady ones focus on the diagonal, there are a few oscillatory cases that have reached their equilibrium location not exactly on the diagonal but rather close to it, which is also observed in other works [59], [69]. As capsules become stiffer, they tend to focus farther from the channel center [77], [78]. Moreover, it is apparent from this figure that the y and z positions of the capsule are also oscillatory in addition to the x position as shown in Fig. 2.2(a). Therefore, all the equilibrium points reported in Fig. 2.2(c) are the average values in each corresponding oscillatory cycle of the trajectory.

It is important to note that we have shown that the numerical results are independent of the distance between 2 consecutive capsules in an infinite domain in the X-direction. This has been done by comparing the distance of the capsule from the center at $Re = 10$, $La = 50$, and $\omega^* = 0.1$ for three different distances of $4W$, $6W$, and $8W$ between 2 consecutive capsules in the X-direction. The maximum difference between the capsule distances from the center for $L = 4W$ and $L = 6W$ is 0.65% or $0.002W$, and the one between those of $L = 4W$ and $L = 8W$ is 0.77% or $0.002W$. The results have also been shown to be mesh independent, by comparing the focal positions for the case of $Re = 10$, $La = 50$, and $\omega^* = 0.1$ with two different grids of $200 \times 114 \times 114$ and $256 \times 152 \times 152$. The difference between their focusing distances from the center is 2.66% or $0.0085W$. To validate our numerical results, the focusing distance as a function of La has been compared to those of a previously published work [59]. The maximum error observed in the capsule trajectory at different La numbers is 1.15%. This validation has also been done in a previous work [77].

The introduced oscillatory flow is not quasi-steady since there is a phase lag between the imposed pressure gradient and the resultant flow parameters such as the velocity field; this is illustrated in Fig. 2.3 by plotting the mass flow rate against the pressure gradient forming a hysteresis loop. Duo to the fluid inertia, there is a delay for the flow in response to the external oscillatory driving force. This effect is more significant for higher values of frequency [79]. As the frequency decreases, the region becomes narrower and eventually approaches a line (quasi-steady). It can also be concluded that the more the hysteresis is, the lower is the required device length.

The Taylor deformation parameter of the capsule is defined as:

$$D = \frac{L - B}{L + B} \tag{2.8}$$

where L is the principal major axis, and B is the principal minor axis of an equivalent ellipsoidal particle. Fig. 3.4 shows the oscillatory deformation of the capsule [80], [81] over time with a frequency twice the flow oscillation frequency since during each pressure gradient period, the capsule reaches maximum or minimum deformation twice [82]. Fig. 2.5 shows the capsule at these instants of maximum and minimum deformations accompanied by the

corresponding average flow velocity at the location of the capsule, and Fig. 2.6 shows the surrounding flow field on the capsule frame of reference at the instant of maximum flow rate in one cycle near the capsule focal point. The minimum deformation occurs close to the instant when the flow is changing direction since the shear disappears. These two instants of time do not coincide exactly due to the present phase lag between the flow and capsule parameters (pressure gradient and capsule deformation in here) as discussed above. This shift in time increases by increasing the frequency due to the increase in the present hysteresis effect, as discussed earlier. Similarly, the maximum deformation occurs close to the instant of maximum flow rate, when the shear rate is also maximum. Fig. 3.4 also confirms the directionality of the equilibrium point with respect to the frequency, as discussed previously. For the shown case in this figure, the average capsule deformation in each cycle reduces by increasing the frequency due to the reduction in the strength of shear rate [83]. Furthermore, the average deformation decrease as the capsule approaches the center since the shear rate approaches zero, and the capsule surface energy gets closer to its minimum desired value.

2.3.2 Necessary length for microchannel

Effect of capsule deformability

Dynamics of capsules with different deformability have been studied in the channel. La number quantifies the deformability, where a low La denotes a very elastic capsule, whereas a high La corresponds to a more rigid particle. Fig. 2.7 illustrates the distance of the capsule focusing position from the channel centerline for various La numbers. Increasing the La increases the distance, a behavior that is in good agreement with the previously published work by *Raffiee et al.* [77] This is because as the value of La increases, the deformation-induced lift force, which is always towards the center [71], [72] to minimize the surface energy of the capsule, reduces and therefore, the equilibrium position moves farther from the centerline. Furthermore, a relatively short microchannel can be designed for all the aforementioned capsules according to Table 2.1. It can also be seen that increasing La reduces the amplitude of movement, which is because as La increases, capsules approach the wall where the velocity of the flow is lower than the centerline. Therefore, capsules

with higher La have lower average velocity and travel a shorter distance in the channel. This would be beneficial in particle focusing applications where the focusing length is very large due to small lift forces, e.g., small particles. It is worth mentioning that since the migration pattern of the capsule slightly depends on its initial location, a safety factor has to be considered for designing the microchannel based on the values reported in Table 2.1.

Table 2.1. Amplitude of capsule movement at various La numbers for $\omega^* = 0.1$ and $Re = 10$

La	Amplitude of movement at the limit cycle
1	18.67
10	18.65
50	17.59
250	15.89
500	15.45

Effect of channel flow rate

The effect of different flow rates in the channel on the capsule dynamics has been investigated in this section. Fig. 2.8 illustrates the distance of the capsule focal position from the channel center as a function of Reynolds number. Increasing the Re increases the distance from the center, which is in agreement with a previous work [59]. This is because of the increase in the strength of the shear gradient induced force, acting towards the wall. Table 2.2 shows a short necessary device length for all amounts of channel flow rates. It can further be noted that increasing Re shortens the essential device length, which is because as Re increases, capsules approach the wall where the velocity of the flow is lower than that of the center. It is vital to mention that the oscillatory flow does not produce a single focal point for capsule when Re is very high ($Re = 100$ for instance) as in these cases, the capsule oscillates drastically around a particular region rather than a single point due to the considerable variations in the values of both the shear gradient and deformation lift forces. This may force us to limit the system flow rate to some specific threshold to fulfill the purpose of interest.

Table 2.2. Amplitude of capsule movement at various Re numbers for $\omega^* = 0.1$ and $La = 10$

Re	Amplitude of movement at the limit cycle
5	18.81
10	18.65
25	17.98
37.8	17.17

Square wave oscillatory flow

In practice, it is easier to merely switch the direction of the flow in the channel by a control valve in the experiment. Thus, the simulations are also done with a pressure gradient having a square wave function with the same period and same area under the curve as that of the formerly defined cosine wave. This is to assure that the total amount of the external force acting on the fluid is the same for both cases. Hence, they both have the same average acceleration. By plotting the hysteresis loops for both functions, it is found that the square wave has more hysteresis and requires a shorter device, which obeys the same pattern mentioned in the discussion of Fig. 2.3. This result is presented in Table 2.3.

Table 2.3. Amplitude of capsule movement for two types of oscillation functions at $\omega^* = 0.1$, $Re = 10$, and $La = 10$

Function form	Amplitude of movement at the limit cycle
sinusoidal	18.65
square wave	17.97

2.4 Conclusions

We have studied the dynamics of a single deformable capsule in a rectangular microchannel with an oscillatory flow of a Newtonian fluid. We observed that under sinusoidal and square wave pressure oscillations, the equilibrium position of the capsule changes compared to a steady flow case. The change is more prominent for higher flow rates by moving the steady equilibrium location closer to the center of the channel but not exactly at the center. The amount of change in the equilibrium location is also dependent on the frequency of the pressure wave with an intermediate value causing higher change. For the same frequency

and flow rate, the change is maximized at an intermediate capsule deformability. The oscillatory flow also enhances the focusing of micron-sized biological pathogens by significantly decreasing the essential microchannel length, which is not the case for steady flows. This improvement is present for all types of capsules, flow rates, and any type of function or mechanism to produce the oscillatory behavior according to the cases presented in the current study. The effect of varying La and Re numbers on the capsule dynamics was also studied. It was observed that higher flow rates and more rigid capsules shorten the required channel length. We believe that this work is significant because it provides the ability to have more direct control over the migration of cells inside the microchannels, which could be useful for cell sorting and separation, filtering bacteria and fungi, etc.

Acknowledgement

This work is supported by the National Science Foundation (Grant No. CBET-1705371) and by the USDA National Institute of Food and Agriculture (Hatch project 1017342).

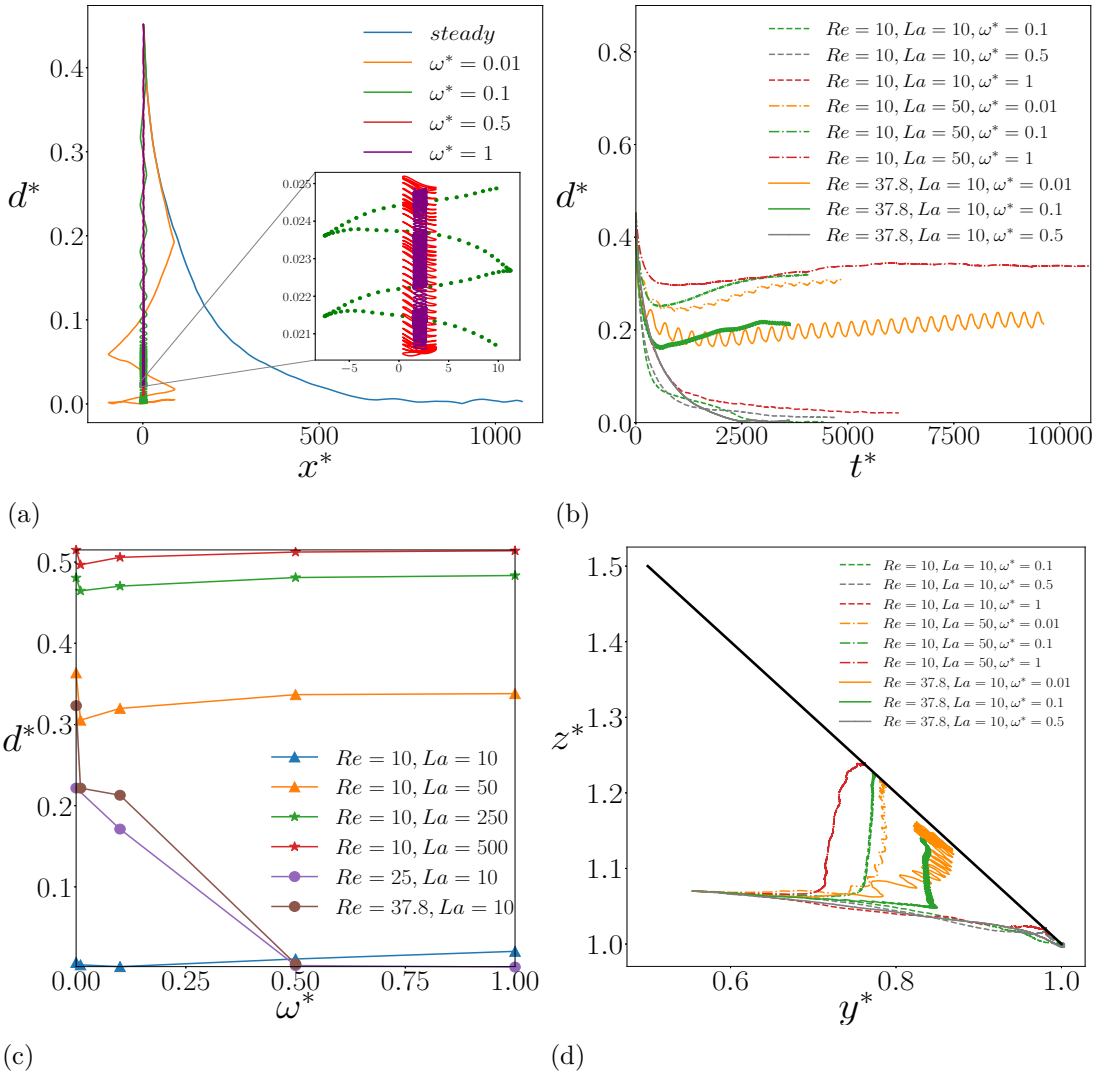

Figure 2.2. Evolution of the capsule motion for different cases by illustrating the time dependent progress in its trajectory (a) versus the flow direction for $Re = 10$ and $La = 10$, (b) versus time, (c) the equilibrium position versus the frequency, and (d) on the channel cross section with the same legend as that of the (b)

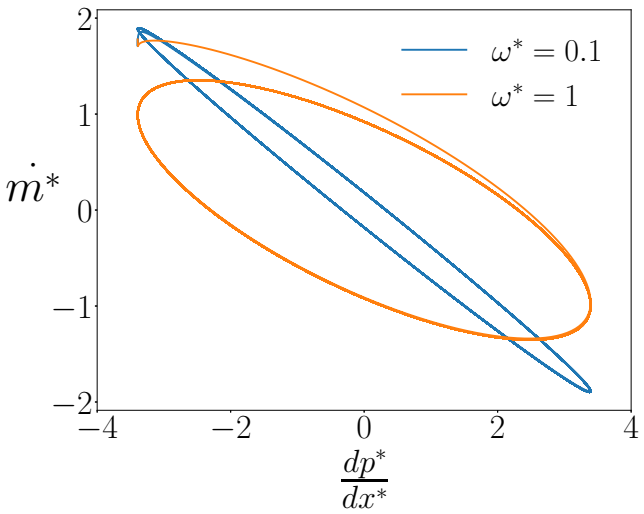

Figure 2.3. Hysteresis loop at two different frequencies for $La = 10$ and $Re = 10$

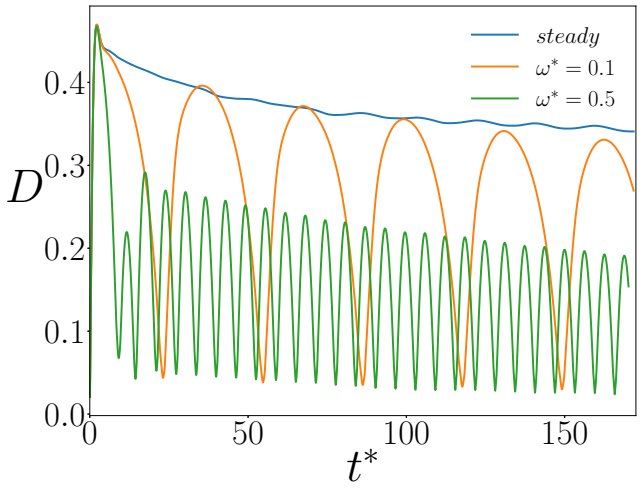

Figure 2.4. Deformation of the capsule at three different frequencies for $La = 10$ and $Re = 37.8$

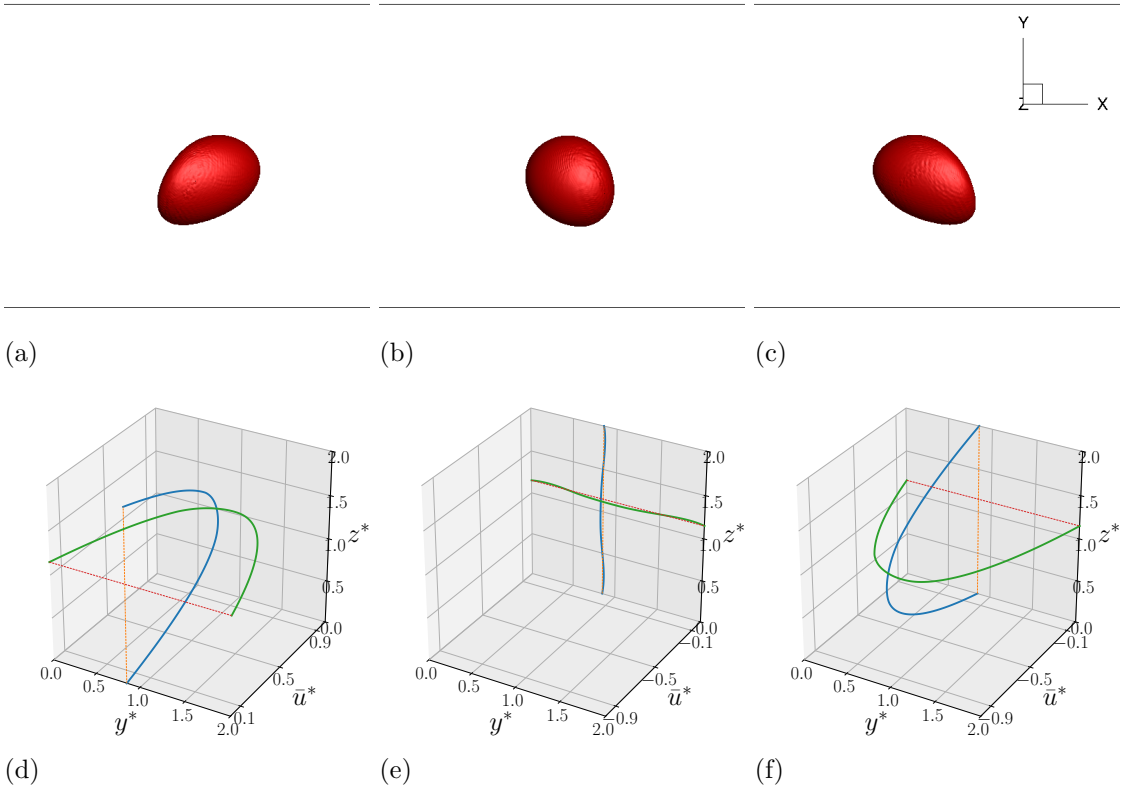

Figure 2.5. Deformed shape of the capsule at $La = 10$, $Re = 37.8$, and $\omega^* = 0.1$ in one cycle close to its focal point when flow is (a) from left to right, (b) changing direction, (c) from right to left, and the corresponding dimensionless averaged velocity profile along the flow direction when flow is (d) from left to right (e) changing direction (f) from right to left

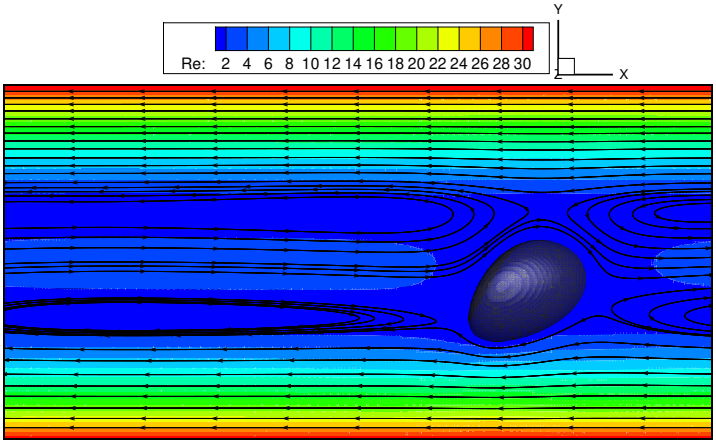

Figure 2.6. Flow field around the capsule on its frame of reference at $t^* = 3269.87$ for $La = 10$, $Re = 37.8$, and $\omega^* = 0.1$ on the xy plane

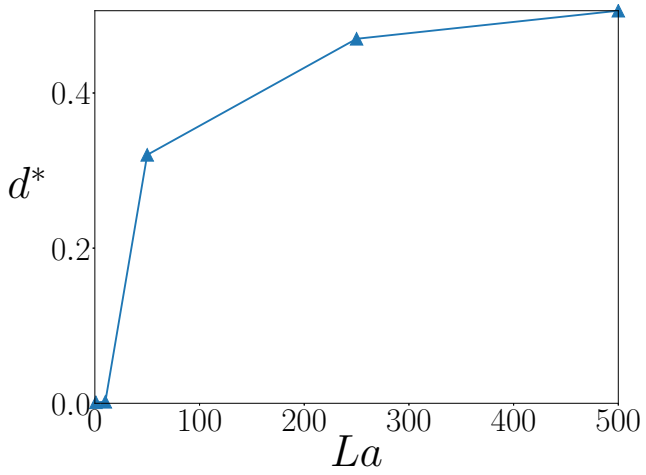

Figure 2.7. Distance of the capsule focusing position from the center at various La numbers for $\omega^* = 0.1$ and $Re = 10$

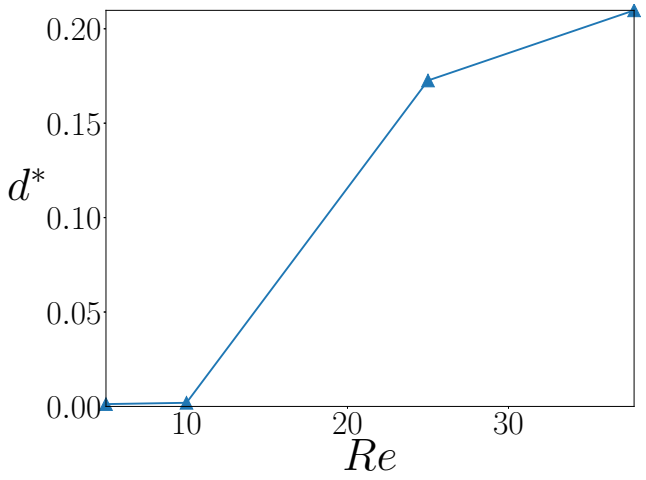

Figure 2.8. Distance of the capsule focusing position from the center at various Re numbers for $\omega^* = 0.1$ and $La = 10$

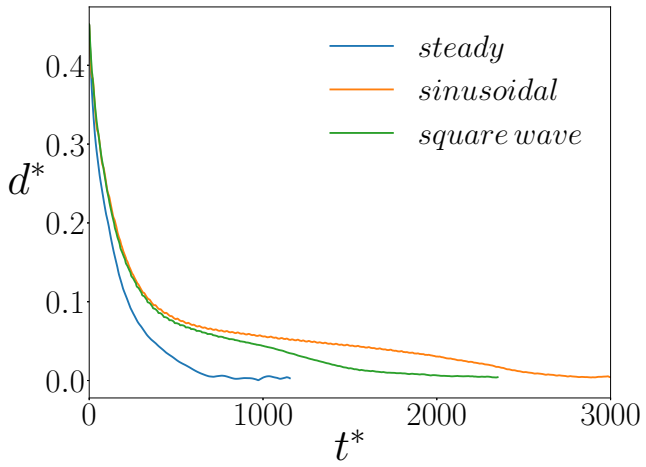

Figure 2.9. Evolution of the capsule motion for two types of oscillatory functions with $\omega^* = 0.1$ and their comparison with the steady case at $La = 10$ and $Re = 10$

3. DYNAMICS OF DROPLET MIGRATION IN OSCILLATORY AND PULSATING MICROCHANNEL FLOWS AND PREDICTION AND UNCERTAINTY QUANTIFICATION OF ITS LATERAL EQUILIBRIUM POSITION USING MULTI FIDELITY GAUSSIAN PROCESSES

3.1 Summary

Dynamics of a droplet in oscillatory and pulsating flows of a Newtonian fluid in a microchannel has been studied numerically. The effects of oscillation frequency, surface tension, and channel flow rate have been explored by simulating the drop within a microchannel. These types of flows introduce new equilibrium positions for the drop compared to steady flows with similar conditions. The simulation results are very sensitive to the grid resolution due to the unsteady behavior of the base flow. Therefore, a set of fine grids have been used in this study to capture the physics of this problem more accurately. However, these fine grids make the computations significantly expensive. Therefore, a Multi Fidelity Gaussian processes method with two levels of fidelity has been used to predict the results of the remaining fine-grid simulations along with their uncertainties based on their correlations with those of the coarse-grid cases over a wide range of input parameters.

3.2 Methodology

3.2.1 The fluid dynamics simulations

A single Newtonian droplet has been placed in a laminar flow of an incompressible Newtonian fluid in a rectangular microchannel with a square cross section. A schematic of the configuration is illustrated in Fig. 3.1(a). The density and viscosity ratios (η and λ, respectively) are set to 1 for most of the simulations. The front-tracking method [60], [84]–[90] is used to update the interface position. In this method, the main governing equations are solved in the fixed Eulerian grid, and the obtained information is used to update the prop-

erties across the droplet surface containing thousands of moving Lagrangian elements. The governing equations to be solved in the entire computational domain are the following:

$$\nabla \cdot \mathbf{u} = 0, \tag{3.1}$$

$$\frac{\partial(\rho \mathbf{u})}{\partial t} + \nabla \cdot (\rho \mathbf{u}\mathbf{u}) = -\nabla p + \nabla \cdot \boldsymbol{\tau} + \iint \gamma \kappa \delta(\boldsymbol{x} - \boldsymbol{x}_{\mathrm{i}}) \mathbf{n} dA, \tag{3.2}$$

where ρ is the density of the fluid, p represents the pressure, $\mathbf{u}$ is the velocity vector, t is the time, $\boldsymbol{\tau} = \mu(\nabla \mathbf{u} + \nabla \mathbf{u}^T)$ is the stress tensor in which μ is the fluid viscosity, κ is the curvature at the interface, γ is the interfacial tension, δ is the Dirac delta function, $\boldsymbol{x}$ is an arbitrary location in the whole computational domain, $\boldsymbol{x}_{\mathrm{i}}$ is such position on the drop interface, and $\mathbf{n}$ is the unit normal vector to a point on the interface. The given delta function is defined as:

$$\delta(x) = \tilde{D}(x)\tilde{D}(y)\tilde{D}(z), \tag{3.3}$$

$$\tilde{D}(x) = \frac{1}{4\Delta}(1 + \cos(\frac{\boldsymbol{\pi}}{2\Delta}(x))), |x| \leq 2\Delta, \tag{3.4}$$

where Δ is the constant Eulerian grid size.

To generate the oscillatory flow, a cosine wave of pressure gradient with a constant amplitude (in the form of $P_0 cos(\omega t)$) is applied along the channel (x direction) to change the direction of the flow symmetrically. For the pulsating case, this pressure gradient has the shape of $P_0(a + bcos(\omega t))$, where a and b are the weights of the steady and oscillatory components, respectively, and $a + b = 1$. The periodic boundary condition is applied in the x direction, and the no-slip condition is applied on the walls in the y and z directions. W and U_0 (channel centerline velocity corresponding to the steady case) are used as the characteristic length and velocity, respectively. In other words, $x^* = \frac{x}{W}$, $u^* = \frac{u}{U_0}$, $t^* = \frac{t}{\frac{W}{U_0}}$, $P^* = \frac{P}{\mu \frac{U_0}{W}}$, $T^* = \frac{T}{\frac{W}{U_0}}$ (where T is the period), and $\omega^* = \frac{2\boldsymbol{\pi}}{T^*}$. Three dimensionless parameters describe and affect the motion of the drop: (i) Reynolds number $Re = \frac{\rho U_0 2W}{\mu}$, expressing the ratio between inertial forces to viscous ones (ii) Capillary number $Ca = \frac{\mu U_0}{\gamma}$, which denotes the ratio of viscous stress to the interfacial tension, where high Ca corresponds to

a highly deformable drop (iii) The dimensionless oscillation frequency (ω^*). The effect of the frequency can also be embedded in the Womersley number $Wo = (\frac{\omega W^2}{\nu})^{\frac{1}{2}}$, where ν is the kinematic viscosity of the fluid. This number compares the transient inertial effects to viscous forces [70]. The blockage ratio of the drop ($\frac{a}{W}$) is constant and equals to 0.3 for most of the cases studied here. The drop is assumed to have a spherical initial shape and is released at $\frac{y}{W} = 0.55$ and $\frac{z}{W} = 1.07$. The initial location of the drop is arbitrary since it does not alter its equilibrium position [33], [91]–[93]. The axes of symmetry have been avoided. A fine grid of $196 \times 114 \times 114$ (high fidelity level) and a coarse grid of $128 \times 76 \times 76$ (low fidelity level) in the x, y, and z directions, , and with 29578 and 13038 triangular elements for the discretization of the droplet (as shown in Fig. 3.1(b)), respectively, is used for the simulations having $Re = 10$. The simulations with higher Re numbers require even a finer grid resolution (Eulerian grid of $256 \times 152 \times 152$ with 48050 Lagrangian elements). Since this adds another level of fidelity to the problem, we have omitted the effect of Re in the second part of the chapter for more simplicity. Therefore, the input parameters that affect the output of interest, which is the distance of the equilibrium position of the drop from the channel center, are reduced to the Capillary number (Ca) and frequency (ω^*).

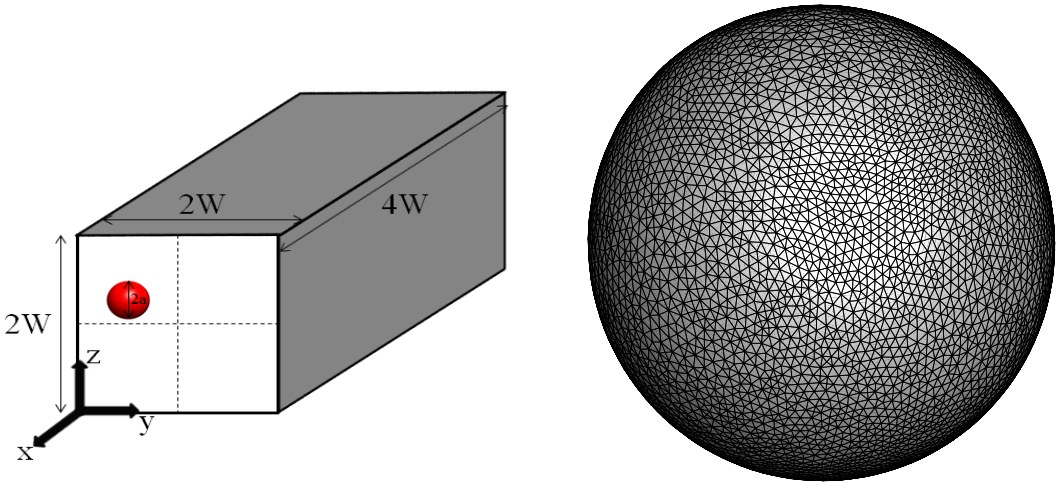

(a) (b)

Figure 3.1. (a) Schematic of the problem setup and (b) An example of the droplet discretization

3.2.2 Multi fidelity GP

Gaussian processes (GP) is an example of a continuous stochastic process in which, a multi-dimensional Gaussian distribution is assigned to the function values at the input points as the prior knowledge. In other words, the value of the function that we are aiming to predict follows a Gaussian probability density at each point:

$$\mathbf{f}_{1:n}|\mathbf{x}_{1:n} \sim \mathcal{N}\left(\mathbf{m}(\mathbf{x}_{1:n}), \mathbf{K}(\mathbf{x}_{1:n}, \mathbf{x}_{1:n})\right), \tag{3.5}$$

$$\mathbf{m}(\mathbf{x}_{1:n}) = \left(m(\mathbf{x}_1), \ldots, m(\mathbf{x}_n)\right), \tag{3.6}$$

$$\mathbf{K}(\mathbf{x}_{1:n}, \mathbf{x}_{1:n}) = \begin{pmatrix} k(\mathbf{x}_1, \mathbf{x}_1) & \ldots & k(\mathbf{x}_1, \mathbf{x}_n) \\ \vdots & \ddots & \vdots \\ k(\mathbf{x}_n, \mathbf{x}_1) & \ldots & k(\mathbf{x}_n, \mathbf{x}_n) \end{pmatrix}, \tag{3.7}$$

Where $\mathbf{m}$ is the mean vector, and $\mathbf{K}$ is the covariance matrix whose elements denote the correlations between the input points. These correlations are quantified by a covariance (kernel) function that encodes our prior belief and knowledge about the targeted function like its continuity, differentiability, etc. The choice of this function is very important for a good prediction; otherwise, we need to have sufficient amount of data to compensate this lack of knowledge. One of the most typical examples for this function is the squared exponential (SE) kernel given below:

$$k(\mathbf{x}, \mathbf{x}') = v \exp\left\{-\frac{1}{2}\sum_{\mathrm{i}=1}^{d}\frac{(x_\mathrm{i} - x'_\mathrm{i})^2}{\ell_\mathrm{i}^2}\right\}, \tag{3.8}$$

In which, v is known as the signal strength, and ℓ_i is the length scale of the i-th input dimension of the GP. In this study, we also use the SE function as we believe the function of interest is continuous and infinitely differentiable.

If we have n observations (training set), consisting of $\mathbf{x}_{1:n} = (\mathbf{x}_1, \ldots, \mathbf{x}_n)$ and $\mathbf{y}_{1:n} = (y_1, \ldots, y_n)$, and n^* test points ($\mathbf{x}^*_{1:n^*}$) that we would like to predict the function values at

$(\mathbf{f}^*_{1:n^*})$, we use the following joint probability, according to the definition of GP, as our prior:

$$p(\mathbf{f}_{1:n}, \mathbf{f}^*_{1:n^*}|\mathbf{x}_{1:n}, \mathbf{x}^*_{1:n^*}) = \mathcal{N}\left(\begin{pmatrix} \mathbf{f}_{1:n} \\ \mathbf{f}^*_{1:n^*} \end{pmatrix} \middle| \begin{pmatrix} \mathbf{m}(\mathbf{x}_{1:n}) \\ \mathbf{m}(\mathbf{x}^*_{1:n^*}) \end{pmatrix}, \begin{pmatrix} \mathbf{K}(\mathbf{x}_{1:n}, \mathbf{x}_{1:n}) & \mathbf{K}(\mathbf{x}_{1:n}, \mathbf{x}^*_{1:n^*}) \\ \mathbf{K}(\mathbf{x}^*_{1:n^*}, \mathbf{x}_{1:n}) & \mathbf{K}(\mathbf{x}^*_{1:n^*}, \mathbf{x}^*_{1:n^*}) \end{pmatrix}\right), \tag{3.9}$$

We then model our likelihood as $p(\mathbf{y}_{1:n}|\mathbf{f}_{1:n}) \sim \mathcal{N}(\mathbf{f}_{1:n}, \sigma^2\mathbf{I}_n)$, which is also a Gaussian distribution centered at the known function values and has a variance of σ associated with the measurements noise. Since our data is from simulations, we can assume the observations are not noisy ($\sigma = 0$ and $\mathbf{y}_{1:n} = \mathbf{f}_{1:n}$). Thus, after performing the Bayes' rule, where $\mathcal{D} = (\mathbf{x}_{1:n}, \mathbf{y}_{1:n})$ is the observed data, we get the posterior distribution for $\mathbf{f}^*$ as below:

$$p(\mathbf{f}^*_{1:n^*}|\mathbf{x}^*_{1:n^*}, \mathcal{D}) = \mathcal{N}\left(\mathbf{f}^*_{1:n^*}|\mathbf{m}_n(\mathbf{x}^*_{1:n^*}), \mathbf{K}_n(\mathbf{x}^*_{1:n^*}, \mathbf{x}^*_{1:n^*})\right), \tag{3.10}$$

Where the posterior mean function is:

$$m_n(x) = m(x) + \mathbf{k}(x, \mathbf{x}_{1:n})\left(\mathbf{K}(\mathbf{x}_{1:n}, \mathbf{x}_{1:n})\right)^{-1}\left(\mathbf{y}_{1:n} - \mathbf{m}(\mathbf{x}_{1:n})\right), \tag{3.11}$$

And the posterior covariance function is:

$$k_n(x, x') = k(x, x') - \mathbf{k}(x, \mathbf{x}_{1:n})\left(\mathbf{K}(\mathbf{x}_{1:n}, \mathbf{x}_{1:n})\right)^{-1}\mathbf{k}^T(x, \mathbf{x}_{1:n}), \tag{3.12}$$

With $\mathbf{k}(x, \mathbf{x}_{1:n}) = (k(x, \mathbf{x}_1), \ldots, k(x, \mathbf{x}_n))$ being the cross-covariance vector.

Multi-fildelity modeling helps accurately predict the output of interest by combining outcomes from the low-fidelity models (simulations with a coarse grid resolution in our case) and fewer data points of the high-fidelity (fine numerical grid) ground truth observations. This approach eliminates the need to run numerous high-fidelity simulations with an expensive computational cost and is effective when there is a high correlation between the outputs of low and high-fidelity models [40]. The MFGP method introduced by *Perdikaris et al.* [40] is fundamentally very similar to that of the *Kennedy and O'Hagan* [94], but it is also capable of capturing the more complex nonlinear cross-correlations between the data. Assuming that

we have s fidelity levels (which is 2 in our case), based on this method, the GP has to be done s times recursively. In other words, the GP is done in its standard, usual way on the first level, and for the next levels, the outputs of the previous level $t-1$ are the inputs for the level t. This is done in the way described below [40]:

$$f_t(\mathbf{x}) = g_t(\mathbf{x}, f_{*t-1}(\mathbf{x})), \tag{3.13}$$

Where $f_{*t-1}(\mathbf{x})$ is the posterior distribution of the previous level $t-1$ evaluated at the $\mathbf{x}$, being the inputs of the current level t. The unknown function g_t follows the description of GP [40]:

$$g_t \sim \mathcal{GP}(f_t|0, k_t((\mathbf{x}, f_{*t-1}(\mathbf{x})), (\mathbf{x}', f_{*t-1}(\mathbf{x}'); \theta_t)), \tag{3.14}$$

According to *Le Gratiet and Garnier* [95], this scheme has the same posterior distribution predicted by the fully coupled scheme of *Kennedy and O'Hagan* [94]. The main requirement of this procedure is that the training sets need to have a nested structure (i.e. $\mathbf{x}_t \subseteq \mathbf{x}_{t-1}$) [40].

Since the posterior distribution of the previous level (f_{*t-1}) and the input ($\mathbf{x}$) are from different spaces, a more structured kernel function, coupling the elements from the same space together, is the following [40]:

$$k_{t_g} = k_{t_\rho}(\mathbf{x}, \mathbf{x}'; \theta_{t_\rho}) \cdot k_{t_f}(f_{*t-1}(\mathbf{x}), f_{*t-1}(\mathbf{x}'); \theta_{t_f}) + k_{t_\delta}(\mathbf{x}, \mathbf{x}'; \theta_{t_\delta}), \tag{3.15}$$

In which k_{t_ρ}, k_{t_f}, and k_{t_δ} are kernel functions parameterized by θ_{t_ρ}, θ_{t_f}, and θ_{t_δ}, respectively. For our application, we have chosen the SE kernel function:

$$k(x, x'; \theta_t) = \sigma_t^2 \exp\left\{-\frac{1}{2}\sum_{\mathrm{i}=1}^{d} \mathcal{W}_{\mathrm{i},t}(x_\mathrm{i} - x'_\mathrm{i})^2\right\}, \tag{3.16}$$

Where σ_t^2 is the variance, and $\left\{\mathcal{W}_{\mathrm{i},t}\right\}_{\mathrm{i}=1}^{d}$ are the Automatic Relevance Determination (ARD) weights associated with the fidelity level t [40].

As previously discussed, the posterior distribution of the first level is obtained by the normal GP. Therefore, it is Gaussian. Nevertheless, this is not necessarily the case for

the next fidelity levels, and we need to propagate the input uncertainty through each step recursively. Thus, after carrying out the Bayes' rule, the posterior distribution for the fidelity level t is given by [40]:

$$p(f_{*t}(\mathbf{x}_*)) := p(f_t(\mathbf{x}_*, f_{*t-1}(\mathbf{x}_*))|f_{*t-1}, \mathbf{x}_*, \mathbf{y}_t, \mathbf{x}_t) = \int p(f_t(\mathbf{x}_*, f_{*t-1}(\mathbf{x}_*))|\mathbf{y}_t, \mathbf{x}_t, \mathbf{x}_*)p(f_{*t-1}(\mathbf{x}_*))d\mathbf{x}_*, \tag{3.17}$$

We can then sample from this distribution.

3.3 Results and discussion

3.3.1 Oscillatory flow

Dynamics of the droplet in an oscillatory flow in the microchannel has been studied, and the effects of Re, Ca, and ω^* have been investigated. Re ranges between 10 and 100, Ca ranges between 0.09 and 10, and ω^* values are chosen such that for a channel with a square cross-section of $100\mu m$ and water as the working fluid at room temperature, the frequency values range between 2Hz and 1600Hz (or a corresponding Wo number between 0.2 and 6.3). Although a maximum frequency of 200Hz is mostly reported in the literature [70], recent works have claimed of generating frequencies of around 1KHz [75]. The equilibrium position of the drop is a result of the competition between the lateral lift forces acting on it, including the wall effect and the deformation-induced lift forces, both acting towards the channel center, and the shear gradient force acting towards the wall [55], [71], [72]. Magnus and Saffman lift forces are often very small compared to the other mentioned components and can be neglected [42], [45], [72]. The boundary wall causes the particle to have rotational and translational velocities different from those of the adjacent fluid, which is caused by an uneven distribution of vorticities around the particle [96], [97]. This induces a higher pressure in the gap between the particle and the wall, which repels the particle away from the wall [72]. The existing curvature of the fluid velocity profile makes the magnitude of the velocity of the fluid on the wall side much higher than the channel center side from the particle frame of reference. This inequality causes a low pressure on the wall side leading to a shear gradient lift force that pushes the particle towards the wall [72]. Following the analytical results of

Chan and Leal [73], the deformability-induced lift force for droplets or bubbles that have a distance higher than their diameter from the wall, which is the case in our simulations, is given by [74]:

$$F_{L,deformation} = Ca_p \mu V_{avg} a (\frac{a}{W})^2 \frac{d}{W} f(\lambda), \tag{3.18}$$

$$f(\lambda) = \frac{128\pi}{(\lambda+1)^3} \left\{ \frac{11\lambda+10}{140}(3\lambda^2 - \lambda + 8) - \frac{3(19\lambda+16)}{14(3\lambda+2)}(2\lambda^2 + \lambda - 1) \right\}, \tag{3.19}$$

Where $Ca_p = \frac{\mu U_0}{\gamma} \frac{a}{W}$ is the drop capillary number, V_{avg} is the average velocity of the carrier fluid across the channel, d is the distance of the drop from the channel center, and λ is the viscosity ratio between the inner and outer fluids.

The code has been validated by comparing the drop deformations at $Ca = 0.2$ and different Deborah numbers with those of the *Aggarwal and Sarkar* [98]. The results are in good agreement with a maximum error of 0.72%. To validate the inertial effects, the focal points of the drop at $Re = 8.25$, $Ca = 0.18$, $\frac{a}{W} = 0.2$ and $Re = 21$, $Ca = 0.14$, $\frac{a}{W} = 0.3$ have been compared with those presented by *Marson et al.* [99]. Our obtained focal points lie within their corresponding uncertainty bands. Furthermore, we have shown that the numerical results are independent of the distance between 2 consecutive drops in an infinite domain in the flow direction. This has been done by comparing the drop trajectory at $Re = 10$, $Ca = 1$, and $\omega^* = 0.1$ for three different channel lengths of $4W$, $6W$, and $8W$ in our simulation setup. The maximum difference between the drop trajectories for $L = 4W$ and $L = 6W$ is $0.0003W$, and the one between those of $L = 4W$ and $L = 8W$ is $0.0005W$. The results have also been shown to be grid independent, by comparing the equilibrium positions for the case of $Re = 10$, $Ca = 1$, and $\omega^* = 0.1$ with two different grids of $196 \times 114 \times 114$ and $256 \times 152 \times 152$. The difference between their focal distances from the center is $0.0009W$.

Figure 3.2 shows the distance of the droplet focal point from the channel center (d^*) at different values of Wo, Ca, and Re. The drop focal point in the steady flow moves towards the center by increasing the Ca due to the increase in the deformation force [91], [92], [100] and shifts towards the wall as Re increases because of the improvement in the strength of the shear gradient force [46], [100], [101]. Since W and ν are constant in this work, ω^* and

Wo are directly related to each other. Hence, we can use them interchangeably. The droplet travels at locations far from the wall; so the wall lift can be neglected in our study [72], [96]. Both deformation and shear gradient lift forces, as the remaining active forces, depend on V_{avg} and d^* that vary as the simulations proceed. The dependence of deformation force on these 2 parameters is apparent from equation 3.18. The parameter d^* and the flow velocity at the drop location affect the magnitude of the difference between the velocities on the wall and center sides from the drop frame of reference. Hence, both d^* and V_{avg} determine the magnitude of the shear gradient force. For non-steady flows, including oscillatory and pulsating ones, V_{avg} is time-dependent. The average of this V_{avg} in each corresponding periodic cycle decreases as the ω^* (or Wo) increases. Consequently, the averages of both forces in one periodic cycle change by changing the Wo value keeping other parameters fixed, leading to different equilibrium positions as we can see in Fig. 3.2. A complete explanation of the relationship between the focal point and parameters like ω^*, Ca, and Re can be found in our previous work [102]. According to this figure, the focal point is closest to the channel center at the highest Wo except for $Re = 10$ and $Ca = 1$ and $Re = 10$ and $Ca = 1.67$. This can be explained based on the shape of the flow velocity profile elaborated below.

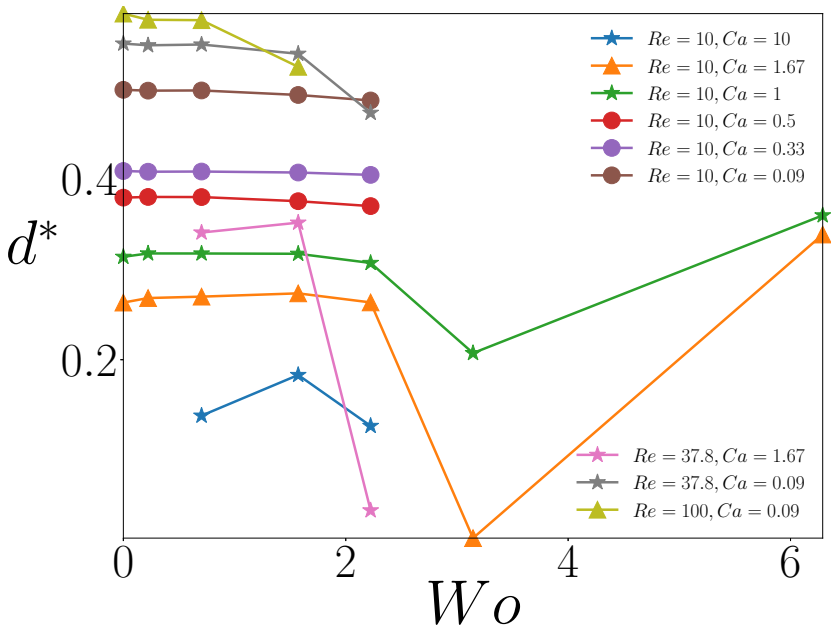

Figure 3.2. Distance of the equilibrium position of the droplet from the channel center as a function of Wo for different cases

Stokes number in the oscillatory and pulsating flows is defined as $St = W\sqrt{\frac{\omega}{\nu}}$. *O'Brien* [103] has solved these types of flows in rectangular channels analytically and quantified the shape of the velocity profile by calculating the ratio between the velocity at the center and its average across the cross-section. Based on the values in table 1 of this chapter, the profile maintains its parabolic shape up to $St = 3$ for a square channel. Above this approximate value, the profile starts to become more like a flat, plug-like profile [103]. Figure 3.3 illustrates the shapes of the dimensionless averaged velocity along the flow direction near the drop focal points at $St = 3$ ($Wo = 3.15$) and $St = 6$ ($Wo = 6.3$). These shapes are consistent with the findings of [103] and [104]. At $Wo = 3.15$ ($\omega^* = 2$) the velocity shape is still parabolic and is similar to those of the lower Wo values. However, this shape changes to plug like at $Wo = 6.3$ ($\omega^* = 8$). The average of V_{avg} at this Wo is the lowest because it has the highest frequency among others. Therefore, the value of deformation force on average is very small according to equation 3.18. However, due to the shape of the velocity profile, the relative flow velocity from the drop frame of reference is very small near the center and very large near the wall. Thus, there is a strong shear gradient force although the average of V_{avg} is small. Consequently, the focal point at $Wo = 6.3$ does not follow the trend observed for the lower Wo numbers and is pushed towards the wall.

Furthermore, by taking a closer look at Fig. 3.3(c), we can see that the velocity has an opposite sign near the wall. Due to the present hysteresis in this type of flow, there is a lag in the response of fluid to the change of flow direction [33], [79].

The Taylor deformation parameter of the drop is defined as:

$$D = \frac{L - B}{L + B} \tag{3.20}$$

In which, L is the principal major axis, and B is the principal minor axis of an equivalent ellipsoidal particle. The parameter D is oscillatory for all the flows in this study except for the steady one. This parameter is proportional to the shear rate, which depends on the flow velocity. As a result, the average of D is lower at higher frequencies [83]. This is reflected in Fig. 3.4 by visualizing the average of D in the corresponding periodic cycle as a function of time. This trend also implies that the amount of oscillations in the deformation is lower

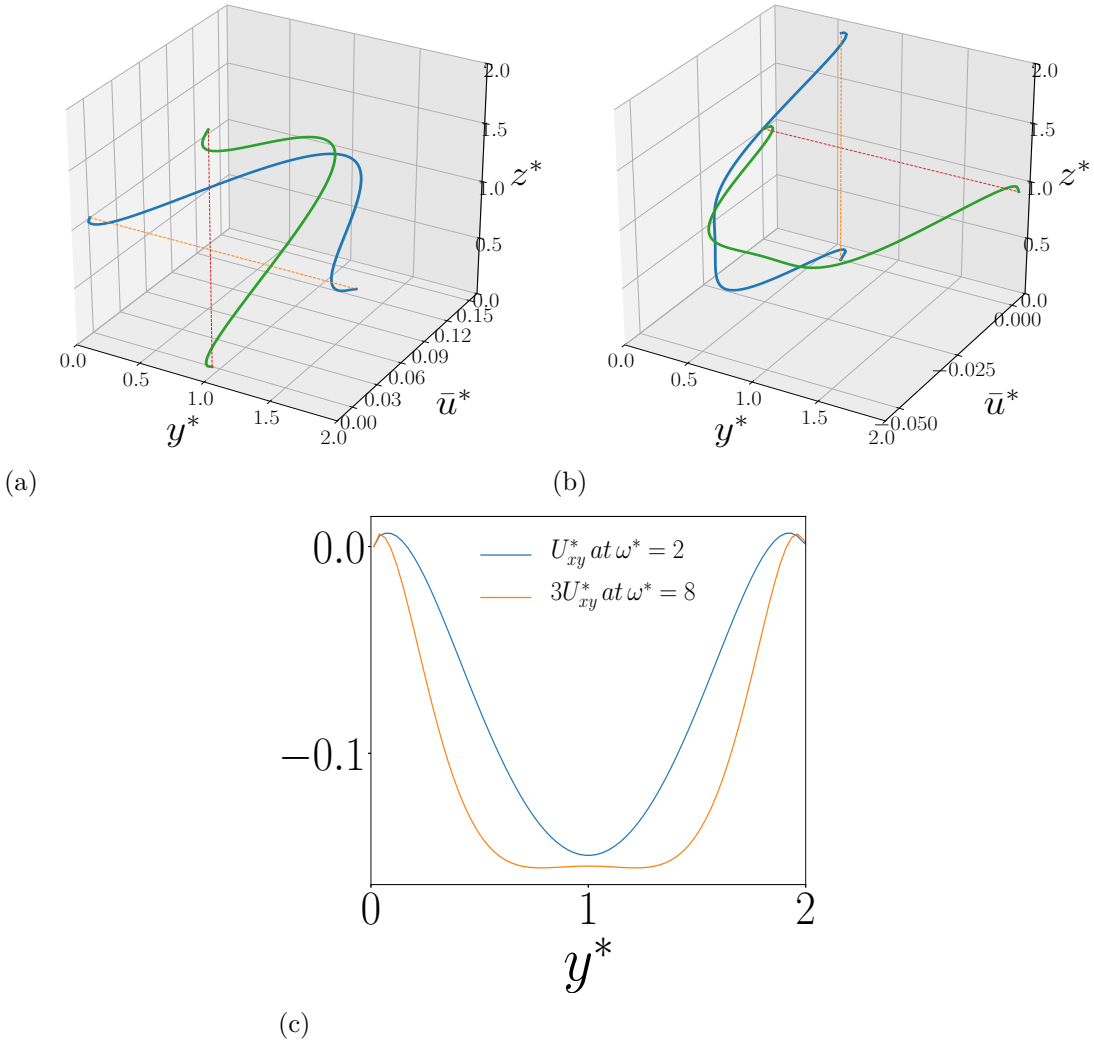

Figure 3.3. Normalized flow direction averaged velocity profiles on the xy and xz planes at $Re = 10$, $Ca = 1.67$, and (a) $\omega^* = 2$ ($Wo = 3.15, St = 3$), (b) $\omega^* = 8$ ($Wo = 6.3, St = 6$), and (c) their shape comparison on the xy plane with the same constant z

at higher frequencies since the minimum deformation in each cycle is zero. Moreover, it is apparent that the case with $\omega^* = 8$ has a deformation of close to 0, which confirms that it has a very low V_{avg}. In fact, the droplet in this case travels about only $0.02W$ along the flow direction and remains almost spherical though the $Ca = 1$ corresponds to a very deformable drop. Nevertheless, it migrates around $0.08W$ from the initial location to its focal point.

Previous works have reported that drops in the flow regimes of high Ca are elongated significantly leading to their break up [91], [92], [99]. This is the reason for the absence of

any data for $Ca = 10$ and $Re = 10$ for steady and lower frequency flows in Fig. 3.2. The drop undergoes a very large deformation in these cases, which is not what it experiences at higher frequencies. A similar argument holds for $Re = 37.8$ and $Ca = 1.67$ since the drop is able to deform more easily at higher Re [105].

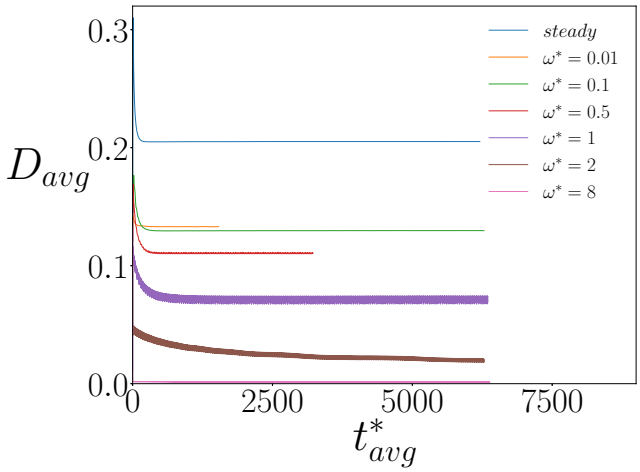

Figure 3.4. Averaged deformation parameter vs averaged dimensionless time at $Re = 10$, $Ca = 1$, and different frequencies

As it was discussed previously, the velocity in the presented type of flows is oscillatory. Consequently, all the active forces also experience fluctuations leading to oscillations in the trajectory of the drop except for the steady flows [33]. This can be seen in Fig. 3.5 where the whole lateral migration patterns at $Re = 10$, $Ca = 1$, and all frequencies, $\omega^* = 1$, and $\omega^* = 0.01$, showing the oscillations in the trajectories are illustrated in figures 3.5(a), 3.5(b), and 3.5(c), respectively, and the amplitudes of oscillations after focusing (A^*) for different cases are depicted in Fig. 3.5(d). In these figures, d^* is the dimensionless, time-dependent distance of the drop from the channel center, and the insets of figures 3.5(b) and 3.5(c) show the trajectory at the last 2 periodic cycles. The plots depicted in the latter 2 figures qualitatively agree with those of a previous study and become more like a helical, spiral pathway as the frequency increases [33]. The minimum velocity in each periodic cycle is zero, occurring when the flow direction changes. The higher average velocity at lower frequencies implies a higher maximum velocity in the corresponding cycle. The higher the difference between the maximum and minimum velocities, the higher is the oscillations

amplitude in the forces and in the trajectory. Therefore, similar to the aforementioned discussion of deformation oscillations, the parameter A^* decreases as ω^* or Wo increases (Fig. 3.5(d)). This is also the case for the oscillations amplitude along the flow direction (the comparison between figures 3.5(b) and 3.5(c)). The existence of these oscillations at all Wo values is noteworthy [33]. It is vital to mention that all the values reported in Fig. 3.2 are the averages of d^* in the last periodic cycle.

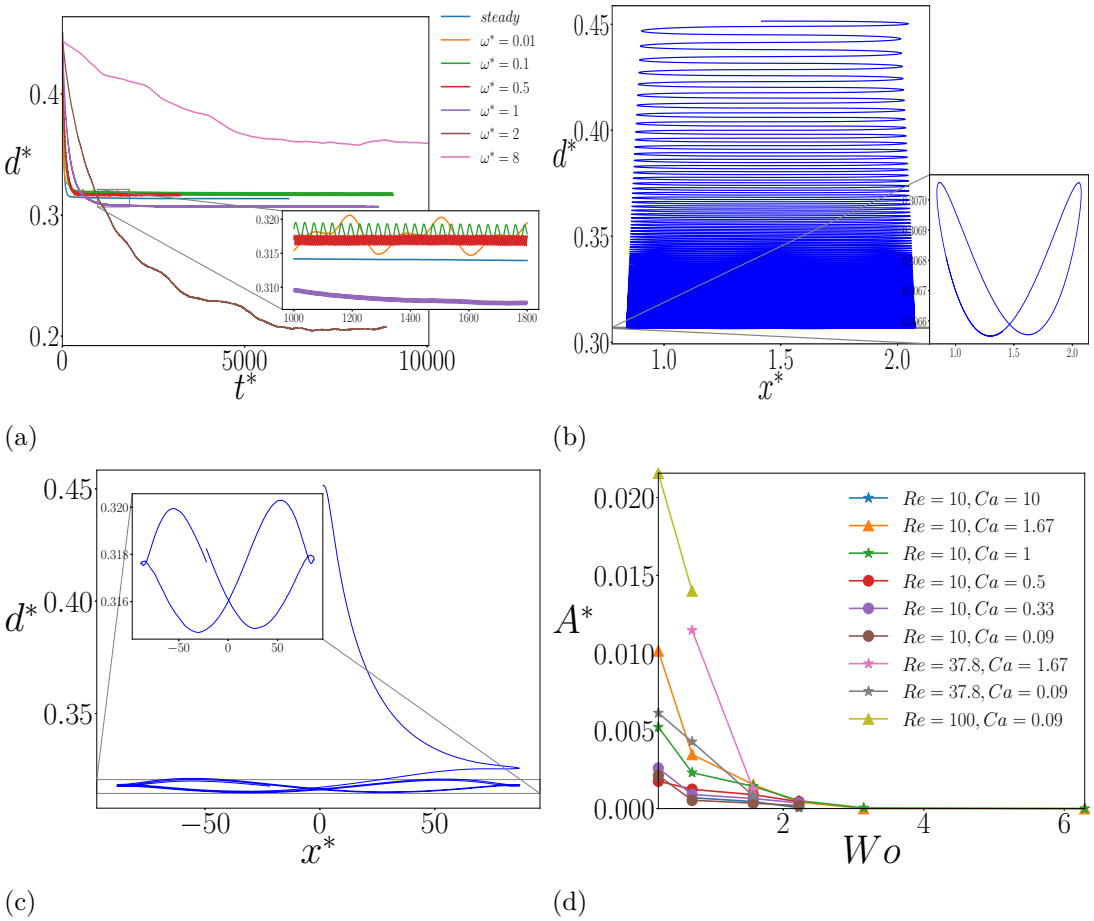

Figure 3.5. (a) Migration patterns at $Re = 10$, $Ca = 1$, and various frequencies, (b) Drop trajectory versus the flow direction at $Re = 10$, $Ca = 1$, and $\omega^* = 1$, and (c) $\omega^* = 0.01$, and (d) Amplitude of oscillations around the equilibrium point after focusing for different cases

Focusing time can be considered as an important factor in the design and performance of the microfluidic system. Nevertheless, it strongly depends on where the particle is initially released. Therefore, the average migration velocity is a better parameter for a more

meaningful comparison under different circumstances. The average migration velocity (v^*) for different cases is shown in Fig. 3.6. This velocity is computed by calculating the distance between the initial and equilibrium positions and dividing it by the focusing time. The corresponding focusing time is determined when the trajectory reaches within $0.015W$ of the focal point. This figure expresses that the average migration velocity decreases as Wo increase. This pattern is also observed in the average velocity along the flow direction. Besides, the average migration velocity in the steady flows increases by increasing the Ca, which is in agreement with the findings of *Alghalibi et al.* [106].

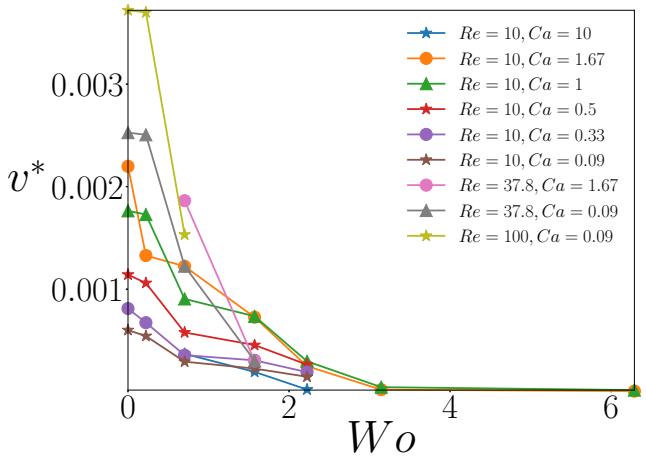

Figure 3.6. The average migration velocity vs Wo

Viscosity ratio in the range of $1 \leq \lambda < 13.2$ has a weak effect on the drop migration [91], [99]. The effect of density ratio (η) on the drop focal point is even less [101]. Therefore, we have limited our study on the effect of these two parameters on the drop migration only to one case as shown in Fig. 3.7. The drop with a λ higher than 1 focuses closer to the wall for the Ca we are studying here [91], [99], [101]. We can also see that the change in the η and λ does not change the distance between the focal points in the steady and oscillatory flows significantly.

3.3.2 Pulsating flow

Changing the steady flow to oscillatory type helps achieve different focal points, which can have potential applications in cell sorting and separation as a great advantage. However,

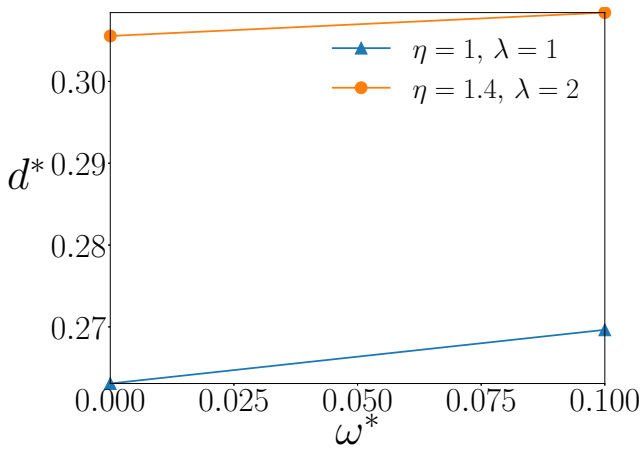

Figure 3.7. The effect of density and viscosity ratios on the distance of the drop focal point from the channel center at $Re = 10$ and $Ca = 1.67$

the oscillatory flow has a zero net flow rate leading to a lower throughput compared to that of traditional steady flows [23], which can be counted as a disadvantage considering many microfluidic applications depending on high-throughput systems. One solution to fix this issue is to combine both steady and oscillatory parts in the pressure gradient and make the flow regime to be pulsating [70]. A pulsating flow has the advantages of having a non-zero net flow rate as well as introducing a new equilibrium point for the drop. The latter occurs because the drop dynamics in the pulsating flow is very similar to the one in a pure oscillatory flow with an equivalent frequency between 0 and that of the oscillatory portion of the pulsating pressure gradient. This claim is valid since the weights of steady and oscillatory portions add up to 1. We can see this equivalent frequency in Fig. 3.8(a) and the inset of Fig. 3.8(c) where the trajectories in the pulsating flows have frequencies of almost half of those of the oscillatory ones with the same frequencies. This feature also enables the existence of cases with high Ca or Re and low ω^* that are absent in the figures of the previous section. This is because the equivalent frequency of the pulsating flow makes the average deformation lower compared to the pure steady flow or oscillatory flow with a lower frequency. It is crucial to mention that the highest weights for the steady portions of the pulsating cases depicted in Fig. 3.8 denote flows in which the drop experiences the highest feasible deformation without breaking up or being significantly elongated. This has been done to show the highest possible changes in the focal points.

In addition, the directionality of the focal points and averages of deformation values obey the expected trend at each combination of Re and Ca in Fig. 3.8. For instance, the pulsating flow at $Re = 37.8$ and $Ca = 1.67$ has an equivalent frequency less than 0.1. Therefore, we can see a focal point closer to the channel center and a higher average deformation according to Fig. 3.8(a) and Fig. 3.8(b), respectively. Similarly, we can observe a focal point closer to the center at $Re = 10$ and $Ca = 10$ for the pulsating case with the larger steady portion. This is because this case has an equivalent frequency between 0.1 and 0.5 and less than the one with the lower steady portion. Fig. 3.8(c) reflects this pattern. The deformation behavior in Fig. 3.8(d) is also qualitatively similar to that shown in Fig. 3.8(b). It is also momentous to pay attention to the $0.012W$ difference between the focal points of the pulsating cases at $Re = 10$ and $Ca = 10$ although the difference between the weights of their steady portions is only 0.01.

Tables 3.1 and 3.2 quantify the average migration velocities for the flow regimes discussed above. The observed trend in these tables is consistent with the information provided in the discussion of Fig. 3.6. The pulsating case at $Re = 37.8$ and $Ca = 1.67$ has the lowest equivalent frequency. Hence, it has the highest average migration velocity among others. Similarly, the v^* at $Re = 10$ and $Ca = 10$ decreases as the equivalent frequency increases.

Table 3.1. Average migration velocities for different flow regimes at $Re = 37.8$ and $Ca = 1.67$

Pressure gradient form	**Average migration velocity**
$P_0(0.93+0.07cos(0.1t))$	0.00191
$P_0cos(0.1t)$	0.00141
$P_0cos(0.5t)$	0.00012

Table 3.2. Average migration velocities for different flow regimes at $Re = 10$ and $Ca = 10$

Pressure gradient form	**Average migration velocity**
$P_0cos(0.1t)$	0.000389
$P_0(0.17+0.83cos(0.5t))$	0.000297
$P_0(0.07+0.93cos(0.5t))$	0.000213
$P_0cos(0.5t)$	0.000205

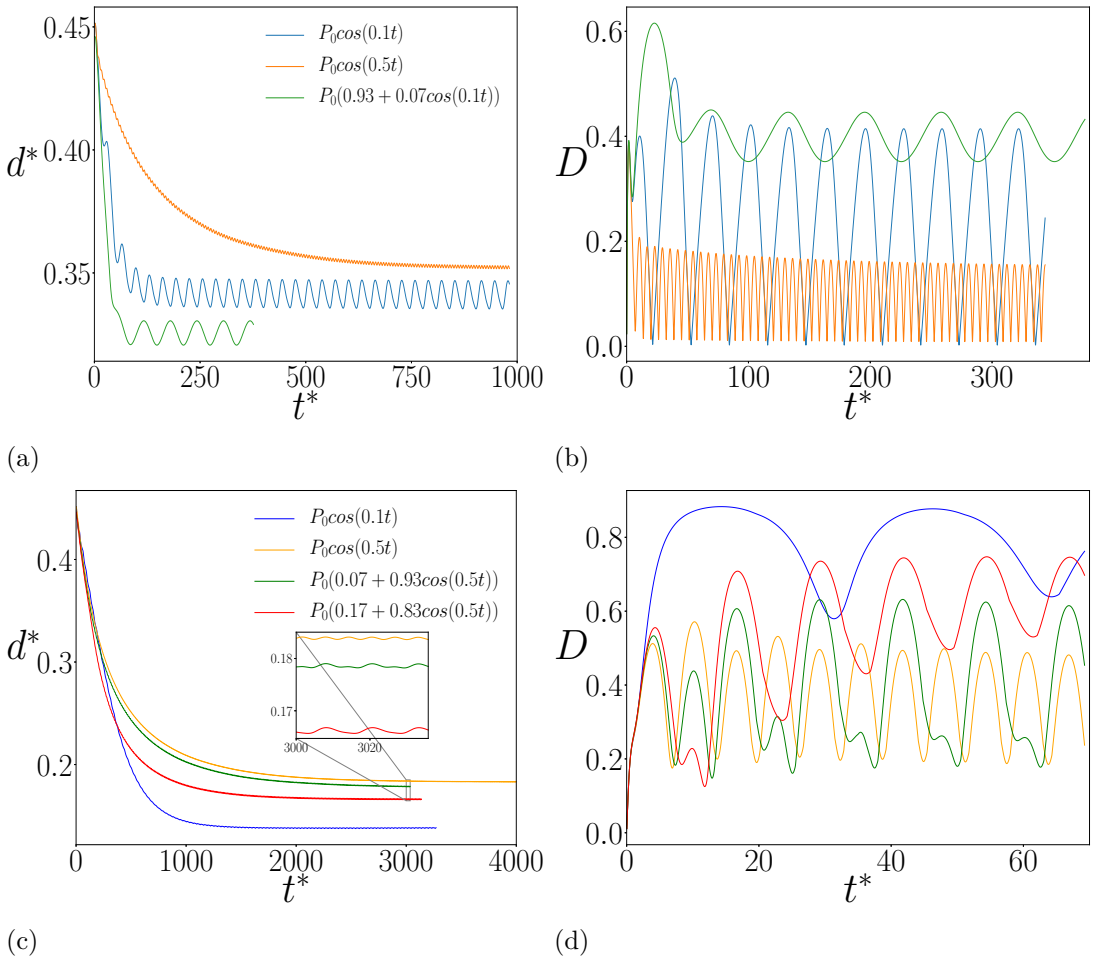

Figure 3.8. Evolution of the oscillatory and pulsating dynamics of the drop at $Re = 37.8$ and $Ca = 1.67$ by illustrating its (a) trajectory, (b) deformation, and at $Re = 10$ and $Ca = 10$ by visualizing the corresponding (c) trajectory, and (d) deformation

The effect of droplet size on its focal point in the oscillatory and pulsating flows at $Re = 10$ and $Ca = 10$ is summarized in Table 3.3. We observe that reducing the drop size pushes its equilibrium location towards the wall [43], [46], [49], [91], [101]. Furthermore, this size reduction appears to enhance the change in the focal point at different values of equivalent frequency.

Table 3.3. The effect of drop size on its focal point at $Re = 10$ and $Ca = 10$

Pressure gradient form	**Equilibrium distance from center**	
	$\frac{a}{W} = 0.3$	$\frac{a}{W} = 0.2$
$P_0 cos(0.1t)$	0.138	0.193
$P_0(0.17 + 0.83cos(0.5t))$	0.166	0.241
$P_0 cos(0.5t)$	0.183	0.266

3.3.3 MFGP

In this section, we evaluate the MFGP performance by having a dataset consisting of 29 low-fidelity and 22 high-fidelity observations. Fig. 3.9 shows all these observations together. It can be seen that the required nested structure, as mentioned earlier, is satisfied. In other words, for any data point in the high-fidelity level, there is a corresponding point in the low-fidelity level. Fig. 3.10 illustrates the predictions on the distance of the drop equilibrium

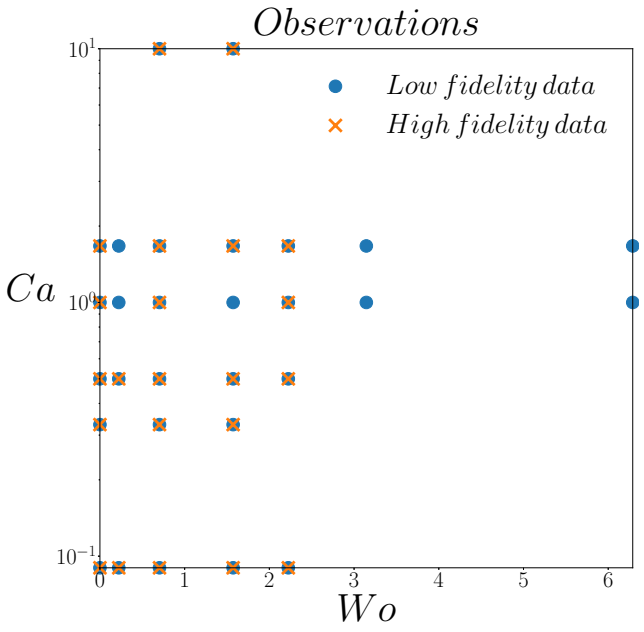

Figure 3.9. Observations of the high and low fidelity levels

position from the channel center over the range of 0 to 1 for the frequency and 0.09 to 1.67 for the Capillary number. The algorithm is trained over the entire available data. A few sanity checks have been done to ensure that these results make sense. First, Fig. 3.10(a) denotes that at any fixed value of the Capillary number, there is a global optimum

frequency for which the equilibrium distance from the center (the z axis) is an extremum. This is also previously observed in the simulations for the input values in the dataset (Fig. 3.2). Secondly, the predictions made by the high-fidelity response are slightly higher than those of the low-fidelity response, which is also compatible with the simulations outcomes. Lastly, we know from the underlying physics that in the steady flow (at a frequency of 0), the distance decreases by increasing the Capillary number [91], [92]. This can be seen in both contour plots of the mean low and high responses (figures 3.10(b) and 3.10(c)) as well as being confirmed quantitatively in the code. Fig. 3.10(d) illustrates a relatively low variance for the high-fidelity response, being our main goal, in the entire domain. The red-colored region in this plot corresponds to places where the density of data points is less, and hence, the predicted outputs have more uncertainty.

Since there is no analytical solution to compare the predictions with, we decided to split the high-fidelity data into training and test sets in this section. This helps us evaluate the performance of the implemented MFGP. We assign 15 training and 7 test points at the high-fidelity level randomly. Then, we train the MFGP on the whole low-fidelity data (29 points) and only the training high-fidelity data, and evaluate the predictive responses on the high-fidelity test points, since those are our main targets. We do this entire procedure 500 times to eliminate the dependence of the results on the test points choice. This especially helps us examine the algorithm performance at the regions with less amount of data. After this bootstrapping, the average of the mean squared error (MSE) was 0.00015 and the average of the R^2 score was 0.9858. The successful reproduction of these results is also checked. Fig. 3.11 shows this evaluation at the last (500th) test set. Fig. 3.11(a) expresses the predictions of d^* along with their 95% credible intervals and denotes that the observed data lies within the corresponding uncertainty bars. In this figure, the x axis label (i) denotes the index of each test point. Figure 3.11(b) visualizes the true or known value of d^* versus its predicted value at each test point. This figure illustrates the strength of the model as the plotted points are very close to the line of $y = x$, which is an indication of the agreement between predictions and observations. The exact and predicted correlations between the high and low responses of d^* are also very close to each other according to Fig. 3.11(c). All of these are evidence for the strong and successful performance of the implemented MFGP algorithm.

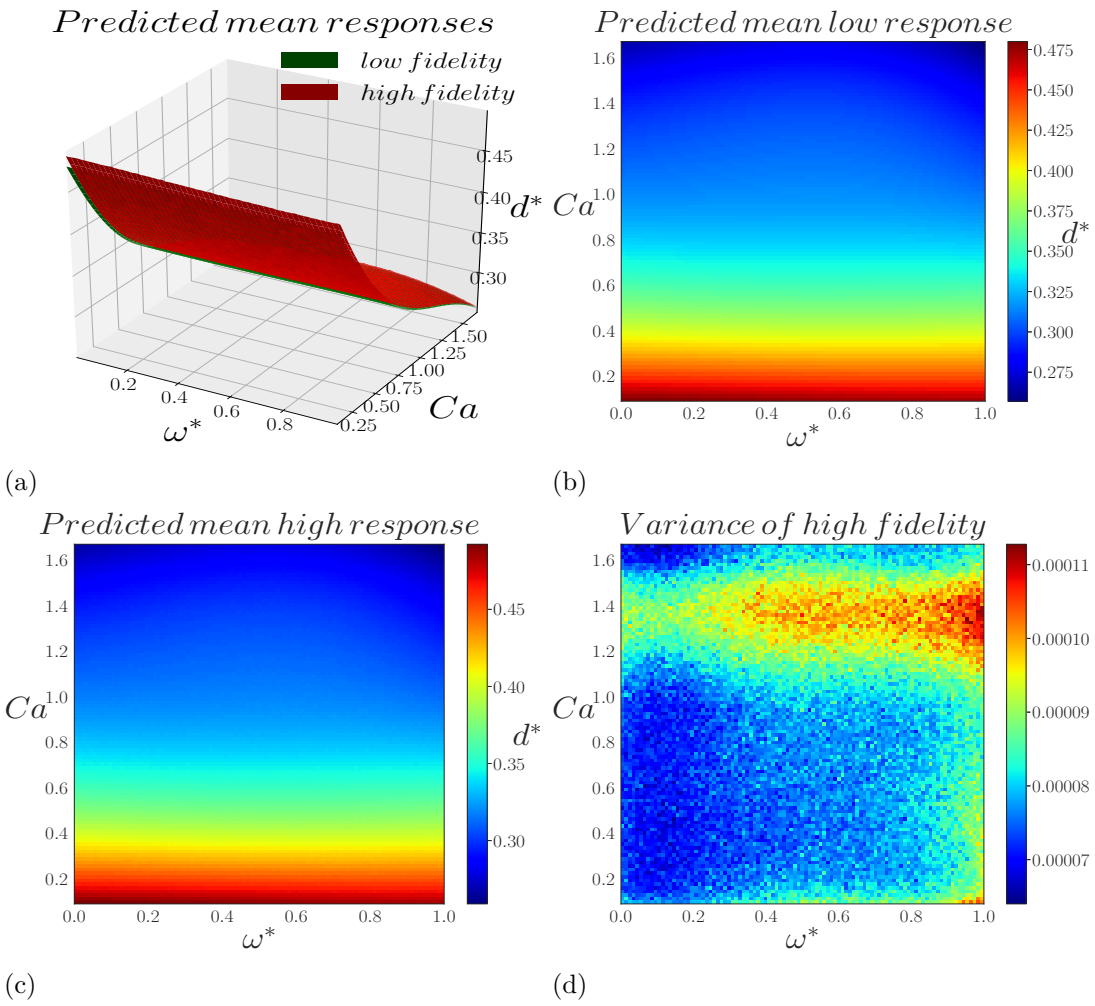

Figure 3.10. Prediction of the MFGP algorithm by illustrating the (a) surface plot of the high-fidelity response colored by red and low-fidelity response colored by green, (b) mean response of the low-fidelity level, (c) mean response of the high-fidelity level, and (d) variance of the high-fidelity response

3.4 Conclusions

Determination and control of the particle's equilibrium position in the microchannels are extremely crucial as it can help in a variety of microfluidics applications. This importance, as well as the need to overcome the issue of designing impractically long channels to work with sub-micron particles, led us to do some simulations to capture the dynamics of a single droplet suspended in an oscillatory flow within the channel. The drawback of the zero net flow rate and smaller throughputs of the oscillatory flow compared to steady one has been

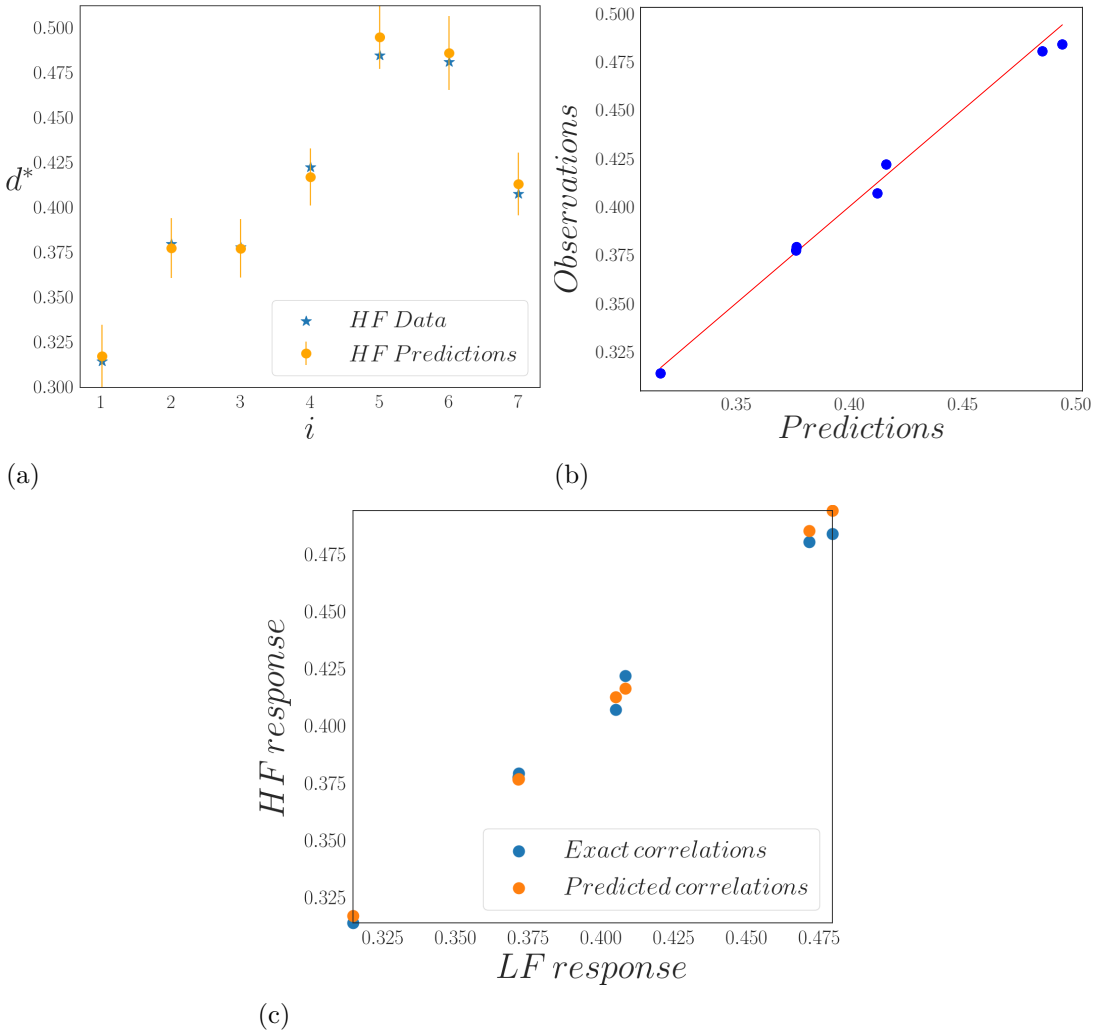

Figure 3.11. Evaluation of the MFGP performance on a random test set by illustrating the (a) observations and predictions with their uncertainties, (b) predictions versus observations, and (c) exact versus predicted correlations

addressed by combining these two to create a pulsating flow regime. Both oscillatory and pulsating flows bring new drop equilibrium locations to the system. Pulsating flows also enable the presence of droplets at high Ca or Re that could break up in the steady or a very low-frequency oscillatory regime. Moreover, fluctuations in the trajectory of the drop have been observed. It has been shown that the amplitude of these oscillations, the average of the oscillatory deformation, and the average migration velocity all decrease by increasing the frequency. The dependence of the drop focal point on the shape of the velocity profile has been investigated as well. It has been explored that this equilibrium position moves

towards the wall in a plug-like profile, which is the case in very high Wo numbers. Due to the significant cost of these simulations, a recursive version of the Multi Fidelity Gaussian processes has been used to replace the numerous high-fidelity simulations that cannot be afforded numerically. The MFGP algorithm is used to predict the equilibrium distance of the drop from the channel center for a given range of the interplaying input parameters, namely the Capillary number and frequency, assuming a constant Reynolds number. In addition, its performance was evaluated by randomly shuffling the high-fidelity data 500 times and assigning 31.8% of it as the test set for an accurate quantitative comparison each time. The algorithm outputs high statistical scores, which is an indication of its reasonably accurate performance.

Acknowledgement

This work is supported by the National Science Foundation (Grant No. CBET-1705371) and by the USDA National Institute of Food and Agriculture (Hatch project 1017342).

4. A NUMERICAL LIFT FORCE ANALYSIS ON THE INERTIAL MIGRATION OF A DEFORMABLE DROPLET IN STEADY AND OSCILLATORY MICROCHANNEL FLOWS

4.1 Summary

Inertial migration of deformable particles has become appealing in recent years due to its numerous applications in microfluidics and biomedicine. The physics underlying the motion of these particles is contingent upon the presence of lift forces in microchannels. Therefore, in this work, we present a lift force analysis for such migration of a deformable droplet in steady and oscillatory flow regimes and identify the effects of varying Capillary number and oscillation frequency on its dynamics. We then propose an expression that mimics the lift force behavior in oscillatory flows accurately. Finally, we introduce a procedure to derive and predict a simple expression for the steady and averaged oscillatory lift for any given combination of Capillary number and oscillation frequency within a continuous range.

4.2 Methodology

A single droplet with density and viscosity ratios of one is placed in a laminar flow of an incompressible Newtonian fluid in a microchannel as illustrated in Fig. 4.1. The drop dynamics is simulated using Front-tracking method [60] as elaborated in detail in our previous work [107]. The pressure gradient in the x direction has a constant magnitude of P_0 for the steady flow and a varying strength of $P_0 cos(\omega t)$ for the oscillatory flow. The periodic boundary condition is applied in the x direction, and the no-slip condition is applied on the walls in the y and z directions. Parameters W and U_c (maximum velocity of the steady case) are used as the characteristic length and velocity, respectively. In other words, $x^* = \frac{x}{W}$, $u^* = \frac{u}{U_c}$, $t^* = \frac{t}{\frac{W}{U_c}}$, $P^* = \frac{P}{\mu \frac{U_c}{W}}$, $T^* = \frac{T}{\frac{W}{U_c}}$ (where T is the period), and $\omega^* = \frac{2\pi}{T^*}$. Three dimensionless parameters describe the dynamics of the drop: (i) Reynolds number, $Re = \frac{\rho U_c 2W}{\mu}$, where ρ and μ are the density and viscosity, respectively, (ii) Capillary number, $Ca = \frac{\mu U_c}{\gamma}$, in which γ is the surface tension, and (iii) the dimensionless oscillation frequency (ω^*). The drop has a constant size of $\frac{a}{W} = 0.3$ with a spherical initial shape, and $Re = 10$

in our entire study. The numerical grid is generated using $196 \times 114 \times 114$ cells in the x, y, and z directions, respectively, and with 29578 triangular elements for the discretization of the drop interface.

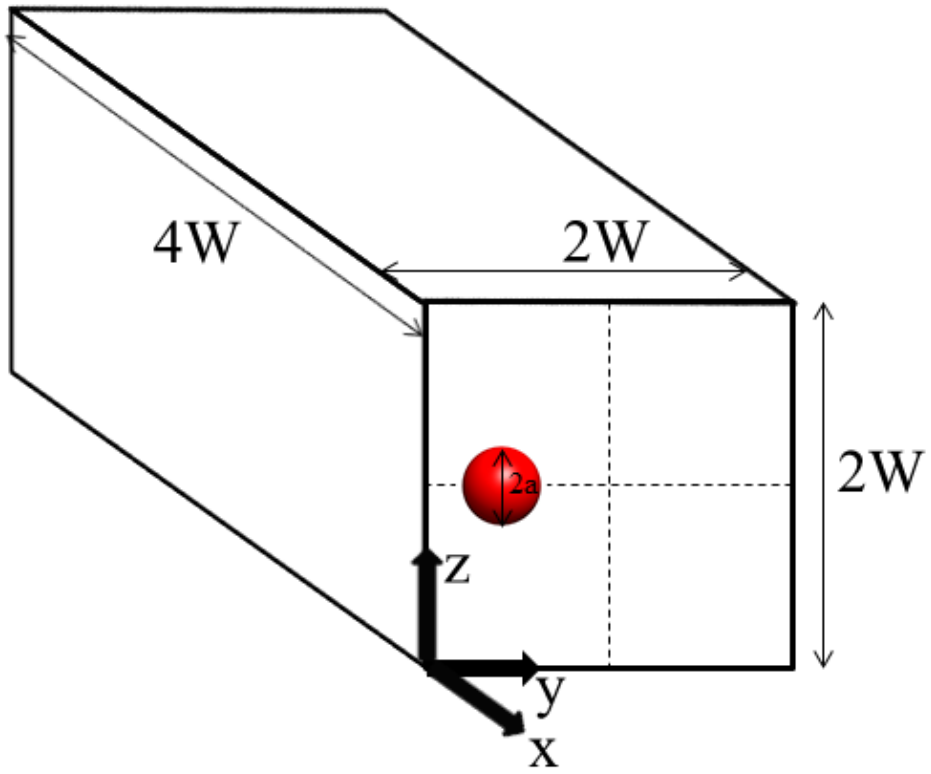

Figure 4.1. Schematic of the problem setup

The active dominant forces on the migrating drop in the wall-normal direction are the inertial and deformation-induced lift and lateral drag forces [42], [45], [72], [108]. The direction of the inertial lift at drop locations far from the wall is towards it, and the deformation lift pushes the drop towards the channel center [55], [71], [72], [108]. The direction of the lateral drag is the opposite of its migration velocity, assuming that the carrier fluid is stationary in the wall-normal direction. Therefore, if we assume the positive direction to be the one from the center to the wall, the force balance on the drop according to Newton's second law is the following:

$$F_{total} = F_{inertial} - F_{deformation} - F_{drag}, \tag{4.1}$$

The drag force is computed based on its definition [109]:

$$F_{drag} = \frac{1}{2} C_D \rho v_r |v_r| A_d, \tag{4.2}$$

$$C_D = \frac{24}{\mathrm{Re}_{rel}} (1 + 0.1 \mathrm{Re}_{rel}^{0.75}), \tag{4.3}$$

$$\mathrm{Re}_{rel} = \mathrm{Re} \frac{v_r}{U_c} \frac{a}{W}, \tag{4.4}$$

Where C_D is the drag coefficient, v_r is the relative velocity between the drop and the fluid (which is essentially its migration velocity), and A_d is the frontal projected area of the drop. Equation 4.3 is consistent with the findings of [109]–[113] and those of [114] at a viscosity ratio of one. Although eq. 4.3 is derived for steady flows, researchers have shown that the drag coefficient in unsteady flows depends heavily on an unsteady parameter that includes the density ratio [115], [116]. Since the density ratio in the present study is one, the aforementioned unsteady parameter becomes zero, and hence, C_D for unsteady flows (including oscillatory cases) can be approximated as the one for steady flows using this equation. The parameter A_d is calculated based on the projected area of the drop on a plane having a normal vector parallel to its migration velocity. Thus, the value of this parameter varies at different instances. This procedure leads to a more precise computation of the drag force.

Considering a viscosity ratio of one, the deformation-induced lift for a drop that has a distance higher than its diameter from the closest wall leads to the following compact form [73], [74]:

$$F_{deformation} = 75.4 Ca_p \mu V_{avg} a (\frac{a}{W})^2 \frac{d}{W}, \tag{4.5}$$

Where $Ca_p = Ca \frac{a}{W}$ is the drop capillary number, V_{avg} is the average velocity of the carrier fluid across the channel, and d is the distance of the drop from the channel center. The linear dependency of this force with respect to the distance d in the specified region is also confirmed in [55].

The lift force analysis in this work is solely based on the drop trajectory. Therefore, to get a lift profile that spans a wide range of d, the drop is released from two different initial locations:

- $y^* = 0.46$ and $z^* = 1$ (the upper release)
- $y^* = 0.98$ and $z^* = 1$ (the lower release)

The upper release is chosen such that the whole range of studied d falls within the validity domain of the deformation force equation (eq. 4.5). This enables us to plug eq. 4.5 into the force balance equation (eq. 4.1) to get the inertial force once the total force is calculated as elaborated below. We will compare the inertial force at different Ca values for the steady flows in the results section. The lower release initial location is slightly off from the channel center since it is also an equilibrium point, and if a drop is placed there, it does not move at all [54]. The initial z component for both releases is on the main axis for faster convergence since the drop eventually focuses on the main axes according to our previous work [107]. These different initial locations do not alter the drop equilibrium position [33], [91]–[93]. The results of each parameter computation for both releases will be combined to reflect its overall behavior within the channel cross-section.

The migration velocity and acceleration of the drop is calculated by taking the first and second temporal derivatives from its trajectory numerically. Since time-step varies throughout the simulations to keep the CourantFriedrichsLewy number at 0.9, the following equations are used to obtain the corresponding derivatives [117]:

$$v_r = \dot{d}_{\mathrm{i}} \approx \frac{-h_{\mathrm{i}}}{(h_{\mathrm{i-1}})(h_{\mathrm{i}} + h_{\mathrm{i-1}})} d_{\mathrm{i-1}} + \frac{h_{\mathrm{i}} - h_{\mathrm{i-1}}}{h_{\mathrm{i}} h_{\mathrm{i-1}}} d_{\mathrm{i}} + \frac{h_{\mathrm{i-1}}}{(h_{\mathrm{i}})(h_{\mathrm{i}} + h_{\mathrm{i-1}})} d_{\mathrm{i+1}}, \tag{4.6}$$

$$\frac{dv_r}{dt} = \ddot{d}_{\mathrm{i}} \approx \frac{2\left[d_{\mathrm{i+1}} + \frac{h_{\mathrm{i}}}{h_{\mathrm{i-1}}} d_{\mathrm{i-1}} - (1 + \frac{h_{\mathrm{i}}}{h_{\mathrm{i-1}}} d_{\mathrm{i}})\right]}{h_{\mathrm{i}} h_{\mathrm{i-1}} (1 + \frac{h_{\mathrm{i}}}{h_{\mathrm{i-1}}})}, \tag{4.7}$$

In which $h_{\mathrm{i}} = t_{\mathrm{i+1}} - t_{\mathrm{i}}$, $h_{\mathrm{i-1}} = t_{\mathrm{i}} - t_{\mathrm{i-1}}$, and d_{i} and t_{i} denote the distance from center and time at the current step. Both non-uniform finite difference schemes have a second-order accuracy.

Taking the first derivative from the steady flow trajectory at the lowest Ca ($Ca = 0.09$) results in a very noisy curve that is impossible to interpret. Therefore, we use an accurate non-linear regression by minimizing the sum of squared errors to fit the trajectories with analytical expressions, from which we can take first and second derivatives analytically. The trajectory from the upper release is very similar to an exponential decay. Therefore, we fit a curve with the following form to it:

$$d(t) \approx c\mathrm{e}^{bt} + k, \tag{4.8}$$

Where c, b, and k are all constants that should be determined by curve fitting. The constant k is essentially the drop equilibrium distance from the center. The trajectory from the lower release looks like the sigmoid logistic function. Consequently, we use the following equation as its analytical general form:

$$d(t) \approx \frac{c}{1 + \mathrm{e}^{-b(t-k)}} + offset, \tag{4.9}$$

Where again, c, b, k, and $offset$ are the regressor constants. The regression fits to both trajectories from the upper and lower release have very high R^2 scores of 0.99 as plotted in fig. 4.2. This figure further confirms that the drop focuses at the same d^* regardless of its initial location.

Once the migration acceleration is derived following the aforementioned steps, it will be multiplied by $\frac{4}{3}\pi a^3 \rho$, which is the total constant mass of the drop with the initial spherical shape, to get the total force. By subtracting the calculated drag force from the total force, the total lift force can be obtained.

4.3 Results and discussion

In this section, we report the results of a single deformable droplet simulations in the previously introduced microchannel that contains either steady or oscillatory carrier fluid. As we are interested in studying the effects of oscillation frequency and Capillary number on the lift force, we fix the Re at a value of 10. Ca ranges between 0.09 and 1.67, and for

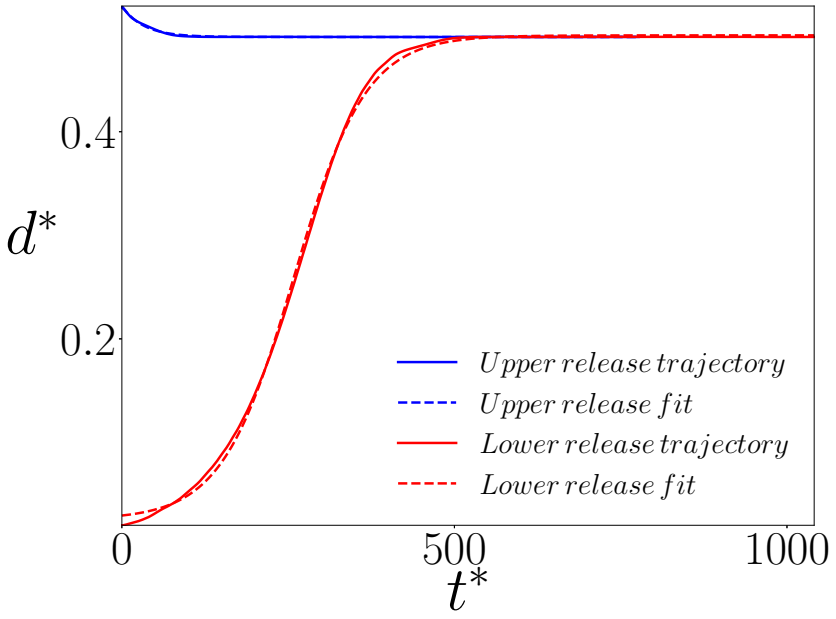

Figure 4.2. Regression fits to both steady trajectories at $Ca = 0.09$

oscillatory cases, ω^* values are chosen such that for a channel with a cross-section of $100\mu m$ and water as the working fluid at room temperature, the frequency ranges between 2Hz and 200Hz, which is mostly referred to in the literature [70]. The validation of our numerical framework, as well as grid and domain independence studies, are discussed in detail in our previous work [107].

Figure 4.3 illustrates the dimensionless mass flow rate over dimensionless time. It can be seen that while the steady regime has the largest constant flow rate in a single direction, the average of oscillatory flow rates in each half of a periodic cycle decreases by increasing the frequency [102], [107]. Although the average of a sinusoidal function in half of a period is constant regardless of its oscillation frequency ($\frac{1}{\frac{\pi}{\omega}} \int_0^{\frac{\pi}{\omega}} sin(\omega t)dt = \frac{2}{\pi}$), the lower maximum absolute value of the flow rate at higher frequencies is the chief reason for the observed phenomenon.

Figure 4.4 visualizes the dimensionless time-dependent frontal projected area of the droplet (parameter A_d in equation 4.2) as it migrates toward its lateral equilibrium position traveling both upper and lower-release trajectories. The first thing we note is that in the transient stage before focusing, the drop has a higher average projected area while trav-

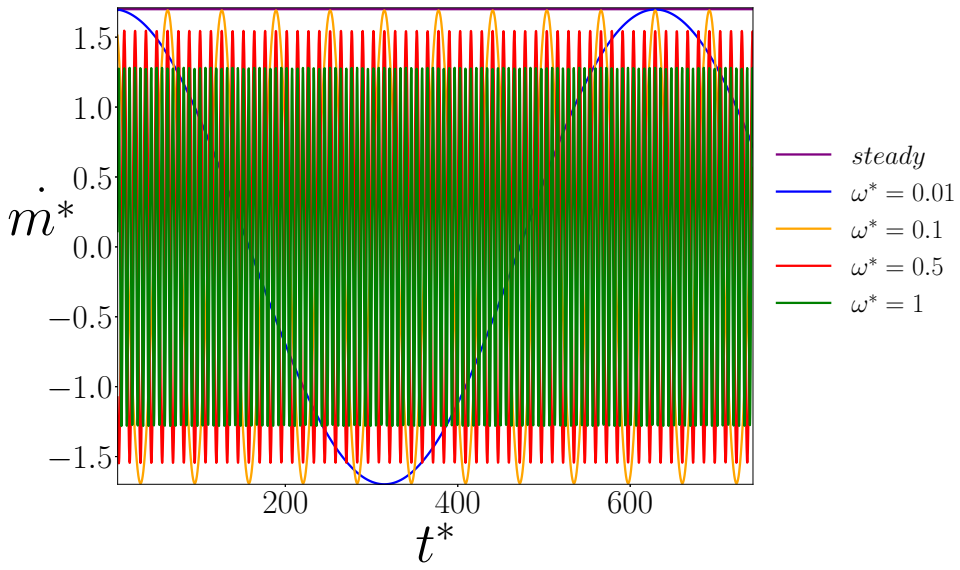

Figure 4.3. Flow rate versus time at $Ca = 1.67$ and $Re = 10$

eling the upper trajectories (fig. 4.4(b)) compared to the one in the lower trajectories (fig. 4.4(a)) in each of the flow regimes correspondingly. This is because the drop experiences more shear and deforms easier when traveling the upper trajectories. Moreover, in each subfigure, the average of A^* is lower at a higher frequency since the average deformation parameter decreases by increasing the frequency [107]. It is important to note that the minimum projected area of the drop in the steady flow is its initial value when the drop is still undeformed and has a spherical shape; in the oscillatory cases, this minimum value occurs when the direction of the flow changes in each periodic cycle. Also, as expected, the drop at higher Ca deforms more and has a higher projected area. This is why $Ca = 1.67$ is used for visualization here among all the other cases in the present study.

Figure 4.5 demonstrates the dimensionless total lift coefficient as a function of the dimensionless distance of the drop from the channel center in the steady flows and at different Ca. Similar to [54], all of the lift coefficients in this work are obtained by dividing the derived lift force, according to the introduced methodology in the previous section, by a factor of $\frac{\pi}{8}\rho V_{avg,s}^2(2a)^2$, in which $V_{avg,s}$ is the average of flow velocity across the channel cross-section in the steady flow. As expected, we observe that each lift curve has a stable equilibrium point at the corresponding drop focal point. Furthermore, at each Ca, the maximum positive

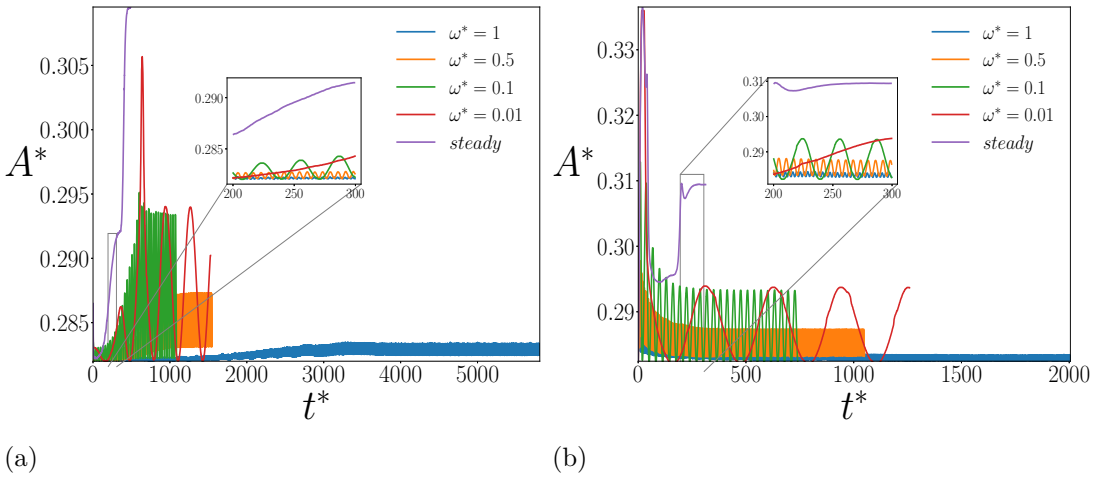

Figure 4.4. Transient cross-stream frontal projected area of the drop when it is released from a (a) lower initial location, and an (b) upper initial location

total lift occurs when the drop migration velocity is also maximum. This maximum value is the highest at the lowest Ca. In addition, the maximum negative total lift is at the initial location of the upper trajectory, and its absolute value is the highest for higher Ca except for $Ca = 1.67$. This is because as we go further up from the channel center and the drop focal point, the deformation lift becomes the dominant force. According to equation 4.5, this force is larger at higher Ca. Also, the negative lift sign in this region is due to the direction of the deformation-induced force, which is toward the center. The drop at $Ca = 1.67$ is released from an initial location closer to the center compared to other cases because it has the highest deformability among all. When it was released from the same location as that of the others, it experienced an extremely large deformation that led to its break up. Therefore, the selected initial point for $Ca = 1.67$ is the furthest possible one from the center that results in the largest possible deformation of the drop throughout its upper trajectory without its break up. Consequently, since the drop in this case starts to travel from a closer distance from the center, it has a lower maximum negative total lift compared to $Ca = 1$ and $Ca = 0.5$ (please refer to eq. 4.5 that shows the dependence of the deformation force on the drop distance from the center).

Since the principal hypothesis underlying equation 4.5 is that the wall effect is negligible due to the large distance of the drop from it [72], [96], [118], we can assume that the shear-

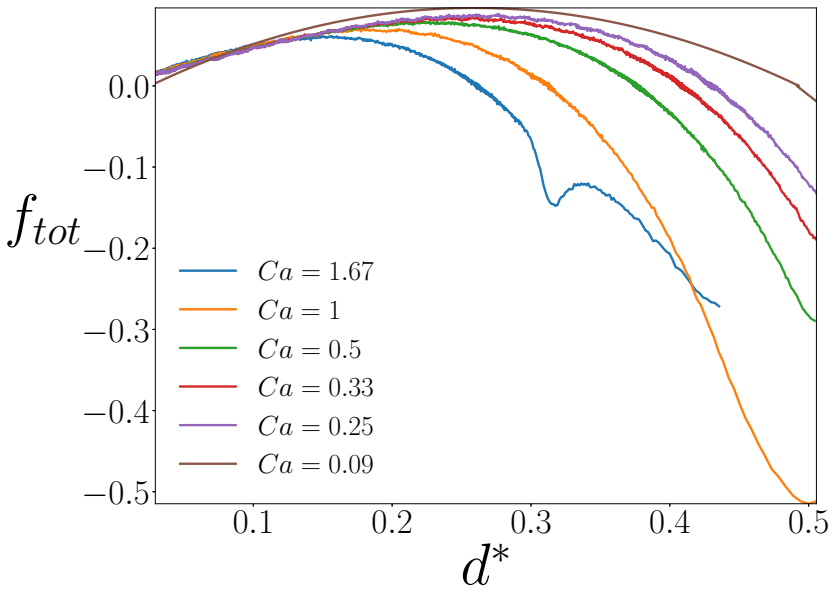

Figure 4.5. Total lift coefficient for the steady flows at different Ca

gradient force is the dominant component of the inertial lift in our study. After subtracting the calculated deformation lift based on this equation from the obtained total lift (fig. 4.5), we can derive the inertial lift, as shown in fig. 4.6. We see that the inertial lift coefficient increases as we increase the Ca number. This could make sense as the more deformed shape of the drop can help further increase the difference between the relative velocities of the fluid with respect to the drop on the channel wall and center sides, which is the chief reason for the shear-gradient force existence [72]. According to eq. 4.5, the deformation force is a linear function of the drop distance from the center and is larger for higher values of Ca. Because of this trivial conclusion, a plot of this force is not depicted here.

Total lift curves acting on the drop in steady and different oscillatory flows at a few Ca numbers are expressed in fig. 4.7. In each subfigure, the higher the drop migration velocity, the larger are both the amplitude of oscillations and the distance between two corresponding points (e.g. maximum or minimum in the oscillatory cycle) on two consecutive periodic cycles. Hence, similar to steady regimes, the maximum absolute values of oscillatory lift coefficients occur when the drop migration velocities are maximum as well. Similarly, the lift oscillations around the drop focal point and near the lower initial point are lower because the drop migration velocities are minimum at those locations.

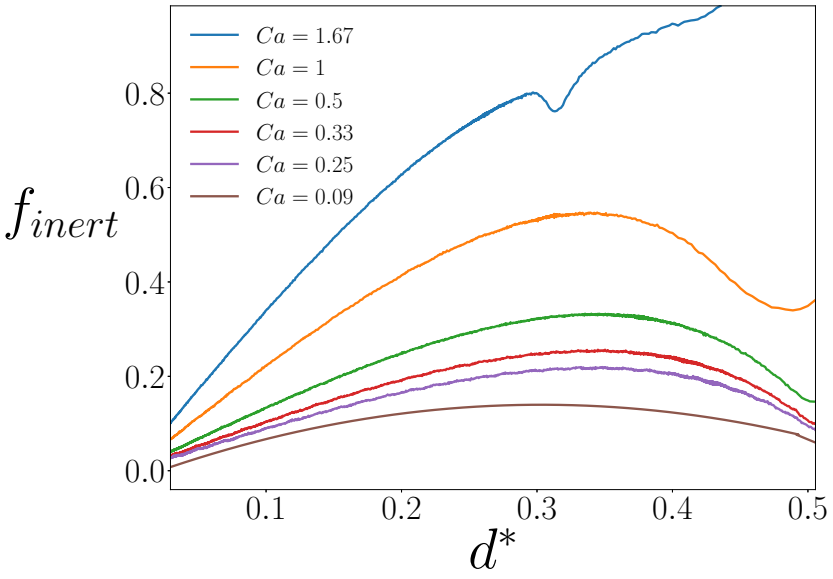

Figure 4.6. Inertial lift coefficient for the steady flows at different Ca

The moving averages of the total lift coefficients in fig. 4.7 are plotted in fig. 4.8. The selected d^*_{avg} while computing the average of lift in each corresponding oscillatory cycle is chosen to be the middle value of d^* in that period. Therefore, since oscillatory cycles with lower frequencies have longer periods, the averaged lift curves at lower frequencies cover a shorter length of d^*_{avg} (a later beginning and a sooner ending). We first note that the obtained averaged lift curves for the oscillatory flows are not necessarily as smooth as that of the steady lift at the corresponding Ca. This observation becomes more pronounced as we increase ω^* or decrease Ca. Nevertheless, these fluctuations on the curves are negligible compared to those of the original oscillatory lifts (fig. 4.7). Additionally, although the average of inertial and deformation-induced lift forces decrease separately by increasing ω^* [107], the difference between them (fig. 4.8) does not follow the same pattern. This confirms the existence of a drop focal point with an extremum distance from the channel center at an intermediate frequency, as elaborated in our previous work [107]. Despite this, the average of lift is the largest in the steady flow and the smallest in the oscillatory flow with the highest frequency at each Ca in our study.

By taking another close look at fig. 4.7, we realize that each of the oscillatory total lift coefficients can be fitted using an expression that comprises of a base curve, which can be

best fitted by a 4th order polynomial, combined with the absolute value of some sinusoidal oscillations. Both the amplitude of oscillations and oscillatory periods can be controlled by the drop migration velocity and have direct relationship with it. In other words, the proposed expression can have the following form:

$$f_{tot} \approx \left\{ m + nv(t) \left| cos\left(\frac{c}{av(t)} d(t) + b \right) \right| \right\} \left\{ gd^4(t) + hd^3(t) + kd^2(t) + ld(t) + q \right\} \tag{4.10}$$

Where $d(t)$ and $v(t)$ are the time-dependent drop distance from the channel center and its migration velocity, respectively, and m, n, a, b, c, g, h, k, l, and q are the constants to be determined while performing the optimization. The constant m is just placed for achieving higher accuracy for the fits, and it ends up to be almost zero compared to other constants in the expression. The resultant curves are plotted in fig. 4.9 against their corresponding data (fig. 4.7(a)) for $Ca = 1.67$ and $\omega^* = 0.01$, $\omega^* = 0.1$, $\omega^* = 0.5$, and $\omega^* = 1$ with R^2 scores of 0.99, 0.99, 0.99, and 0.97, respectively. Similar curves having the same proposed expression with R^2 scores of 0.97 or higher and capable of capturing all the infinitesimal details are obtained for other Ca numbers as well.

To further extend the total lift prediction to more general cases within a continuous range of Ca and ω^*, we consider the steady and averaged oscillatory lifts (fig. 4.8) for regression with a 4th order polynomial here. In other words, the expression in the first bracket of eq. 4.10 is replaced with a value of 1. Using the analytical set of equations 4.11, we can derive the unknown coefficients a, b, c, g, and h of the polynomial analytically. In these equations, the subscripts for d and f denote their locations. For instance, the subscript max represents where the magnitude of total (or averaged) lift is maximum and its first derivative is zero.

The obtained polynomials with this approach have R^2 scores of around 0.9 or higher for the cases presented in fig. 4.8.

$$\begin{cases} ad_{first}^4 + bd_{first}^3 + cd_{first}^2 + gd_{first} + h = f_{first}, \\ ad_{max}^4 + bd_{max}^3 + cd_{max}^2 + gd_{max} + h = f_{max}, \\ 4ad_{max}^3 + 3bd_{max}^2 + 2cd_{max} + g = 0, \\ ad_{\mathrm{eq}}^4 + bd_{\mathrm{eq}}^3 + cd_{\mathrm{eq}}^2 + gd_{\mathrm{eq}} + h = 0, \\ ad_{last}^4 + bd_{last}^3 + cd_{last}^2 + gd_{last} + h = f_{last}, \end{cases} \tag{4.11}$$

Parameters d_{first}, d_{max}, d_{eq}, d_{last}, f_{first}, f_{max}, and f_{last} are already available for the cases in fig. 4.8 to solve the system of equations 4.11 for them. However, we use the multi-fidelity Gaussian processes (MFGP) method to predict these unknown parameters for any given double inputs of $0.25 \leq Ca \leq 1.67$ and $0 \leq \omega^* \leq 1$. MFGP is a Bayesian stochastic approach that does a casual inference on a set of high and low-fidelity datasets, and it is extremely effective if there are strong correlations between them [40]. This method is described in detail in our previous work, and it is carried out to predict the distance of the drop equilibrium position from the channel center (d_{eq}) with R^2 of 0.99 and root mean squared error (RMSE) of 0.01 in that work [107]. Here, we refer to the data for the cases in fig. 4.8 except for $Ca = 1$ as our high-fidelity data. We generate similar data for all the cases in that figure, but with a grid of $128 \times 76 \times 76$ in the x, y, and z directions, respectively, and having 13038 triangular elements for the discretization of the drop. We consider this data as our low-fidelity dataset. Therefore, we have a total of 25 low and 20 high-fidelity data points, which satisfies the required nested structure to apply MFGP on the data [40]. We randomly allocate 5 data points of the entire high-fidelity dataset as our test set since the high-fidelity response is our main target. We train the algorithm on the remaining 40 training data points and evaluate its performance on the test set. We repeat this procedure 30 times and compute the average of evaluation metrics so that the selection of test sets does not significantly affect the overall algorithm performance.

Table 4.1 presents the average of R^2 and RMSE on our 6 remaining unknown parameters after completing the aforementioned steps. We can see that the trained algorithm is capable of predicting the intended parameters with very high accuracies. Especially, the accurate prediction of f_{max} and f_{last} is useful for determining the maximum and minimum values of averaged total lift for any given input in the range, respectively. The slightly less accurate prediction for d_{max} (i.e. where the maximum averaged lift occurs) is because of the present randomness in its values among different cases. This is unlike the consistent pattern that exists for other parameters for a combination of ω^* values across different Ca numbers. The similar lower accurate prediction for d_{last} is due to the lack of data points between $Ca = 1$ and $Ca = 1.67$ since all the cases with $Ca \leq 1$ have the same upper release initial location. However, the R^2 score of around 0.8 for this prediction is still high, and it can help us determine the furthest starting point from the center and the widest traveling region of a droplet with $1 \leq Ca \leq 1.67$ in the microchannel so that it undergoes the largest possible deformation without breaking up.

Table 4.1. MFGP averaged performance metrics on 30 randomly chosen test sets for the parameters required for the determination of the analytical averaged total lift polynomial coefficients

Parameter	$\boldsymbol{R^2}$	**RMSE**
d_{max}	0.79	0.0140
d_{last}	0.78	0.0213
d_{first}	0.97	0.0007
f_{last}	0.92	0.0177
f_{max}	0.99	0.0015
f_{first}	0.99	0.0003

4.4 Conclusions

The dynamics of particles and biological cells in microchannels has caught many researchers' attention because of several biomicrofluidic applications it has. The underlying physics owes its behavior mainly to the presence of different lift forces in such channels. Hence, many scientists have dedicated their time to calculate or measure these forces. However, most of these works have focused on analyzing the lift forces acting on solid and non-

deformable particles and studied the effects of parameters such as particles' size, Reynolds number, etc on them. Consequently, such analysis on deformable droplets or bubbles and studying the effects of varying parameters like Capillary number is almost missing in the literature. In this work, we have extended such analysis to the case of a single deformable droplet in the channel. We have calculated the main components of the lift force based on a unique methodology that merely depends on the drop trajectory. To do so, first, the drop migration velocity and its frontal projected area as it travels its lateral trajectory have been computed to calculate the drag force in the wall-normal direction accurately. After applying Newton's second law on the drop, the total lift profile is obtained over a region where the drop has a distance higher than its diameter from the wall. It has been observed that the total lift has a higher maximum at a lower Capillary, and its minimum decreases as we increase the Ca. The inertial and deformation-induced lift forces both increase by increasing the Ca number. Moreover, since the oscillatory flows within the microchannel were previously shown to enable working with sub-micron biological particles as well as introducing new focal points for them, we have also included these flow regimes in our analysis and investigated the effects of oscillation frequency on the lift in addition to the Capillary number. We have seen that for all cases, the total lift and for oscillatory ones, the amplitude of oscillations are both higher when the drop migration velocity is higher. At each Ca, the steady lift and moving averages of oscillatory ones at different ω^* have also been compared. It has been shown that the steady lift has the largest magnitude, and the average of oscillatory one with the highest frequency in this study has the smallest strength. However, there is not a constant decreasing pattern in the average of lift by increasing the frequency, which is why the drop focuses furthest from the channel center at an intermediate ω^*. Additionally, an accurate mathematical expression has been proposed that captures the detailed total oscillatory lift curves at various ω^* with R^2 scores of 0.97 or higher. Finally, the multi-fidelity Gaussian processes has been used to accurately predict the 7 unknown parameters required to define a simple 4th order polynomial to fit the steady and averaged oscillatory lifts with R^2 scores of about 0.9 or higher for any given Ca and ω^* within the ranges of $0.25 \leq Ca \leq 1.67$ and $0 \leq \omega^* \leq 1$.

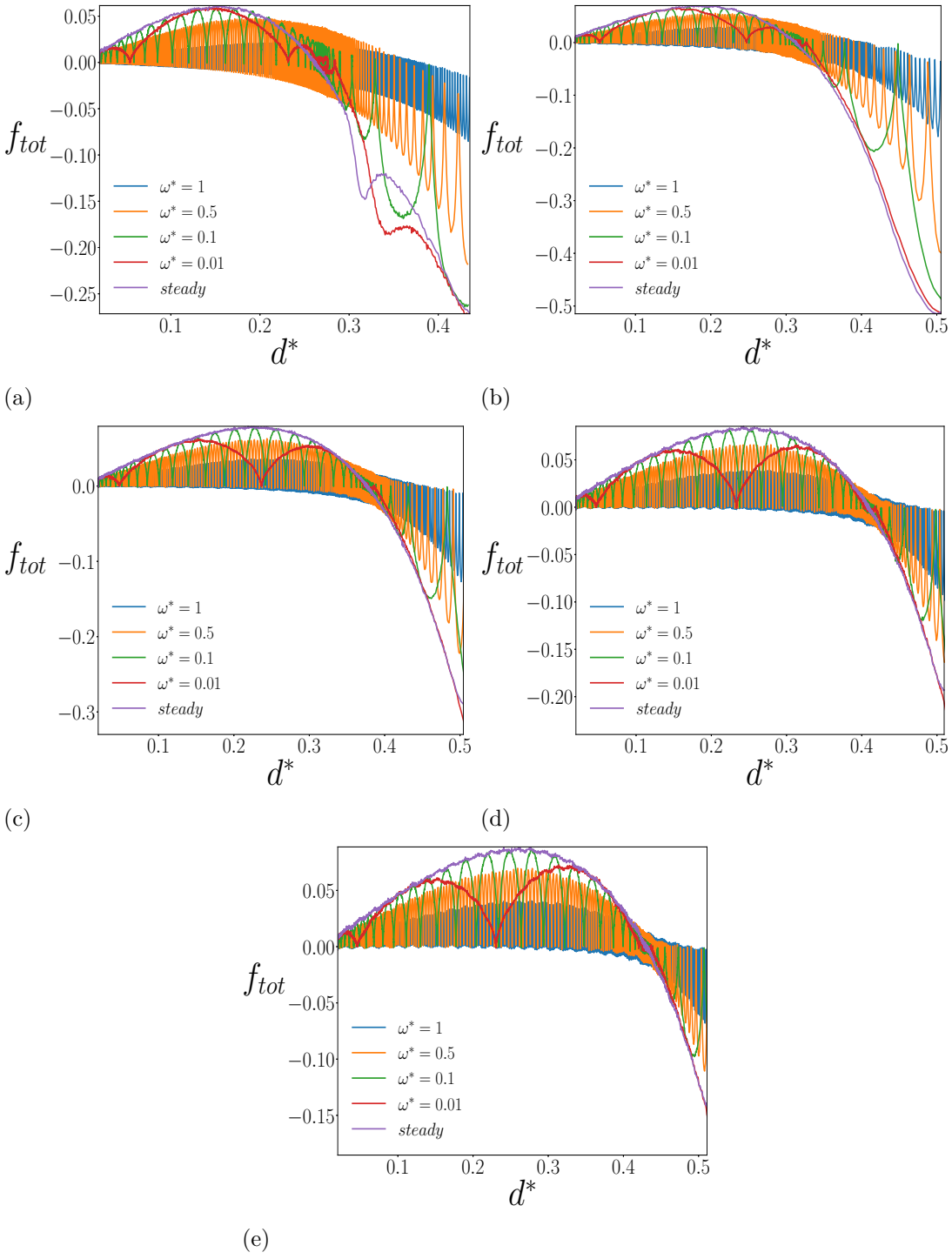

Figure 4.7. Total lift coefficients for steady and oscillatory flows with different frequencies at (a) $Ca = 1.67$, (b) $Ca = 1$, (c) $Ca = 0.5$, (d) $Ca = 0.33$, and (e) $Ca = 0.25$

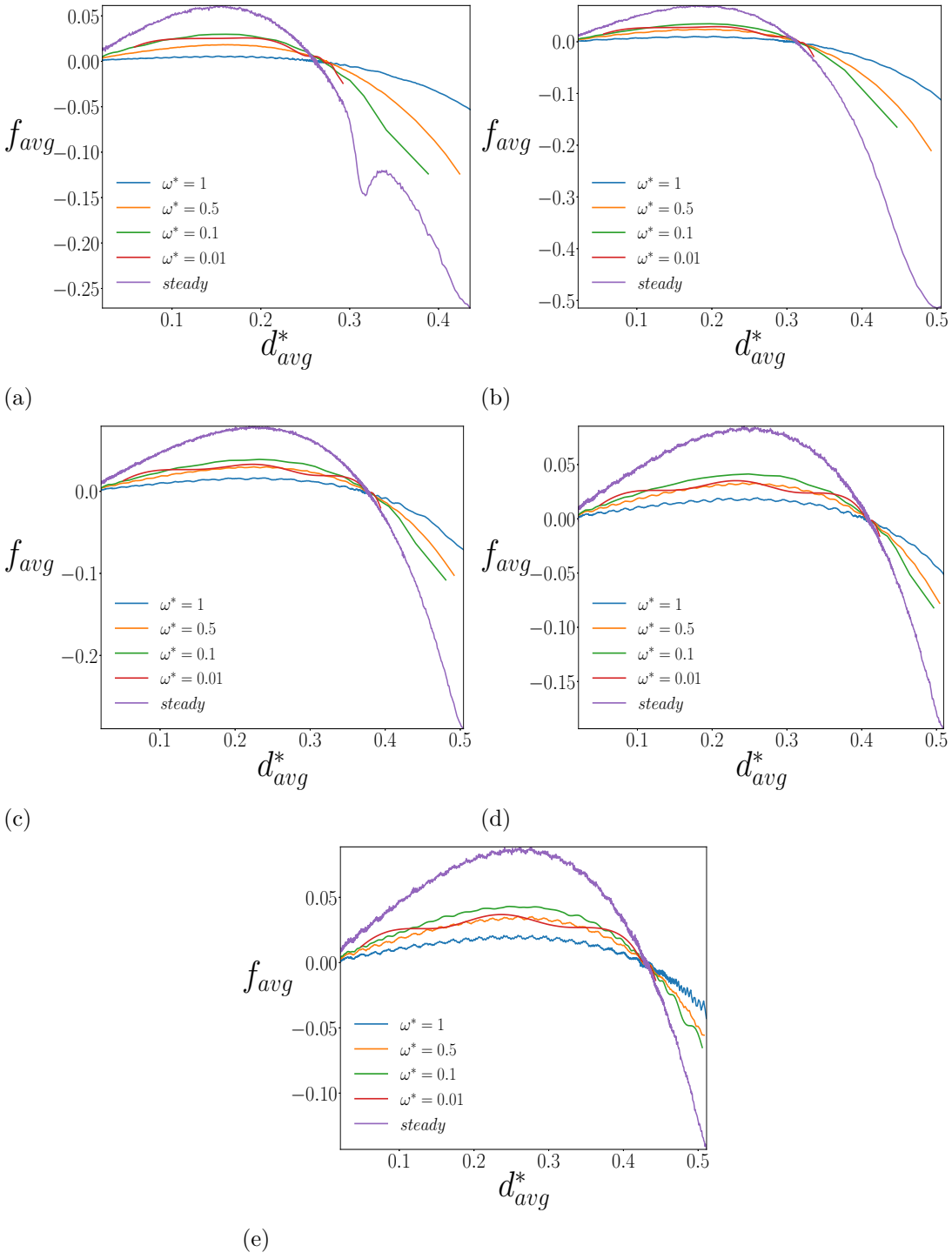

Figure 4.8. Averaged total lift coefficients for steady and oscillatory flows with different frequencies at (a) $Ca = 1.67$, (b) $Ca = 1$, (c) $Ca = 0.5$, (d) $Ca = 0.33$, and (e) $Ca = 0.25$

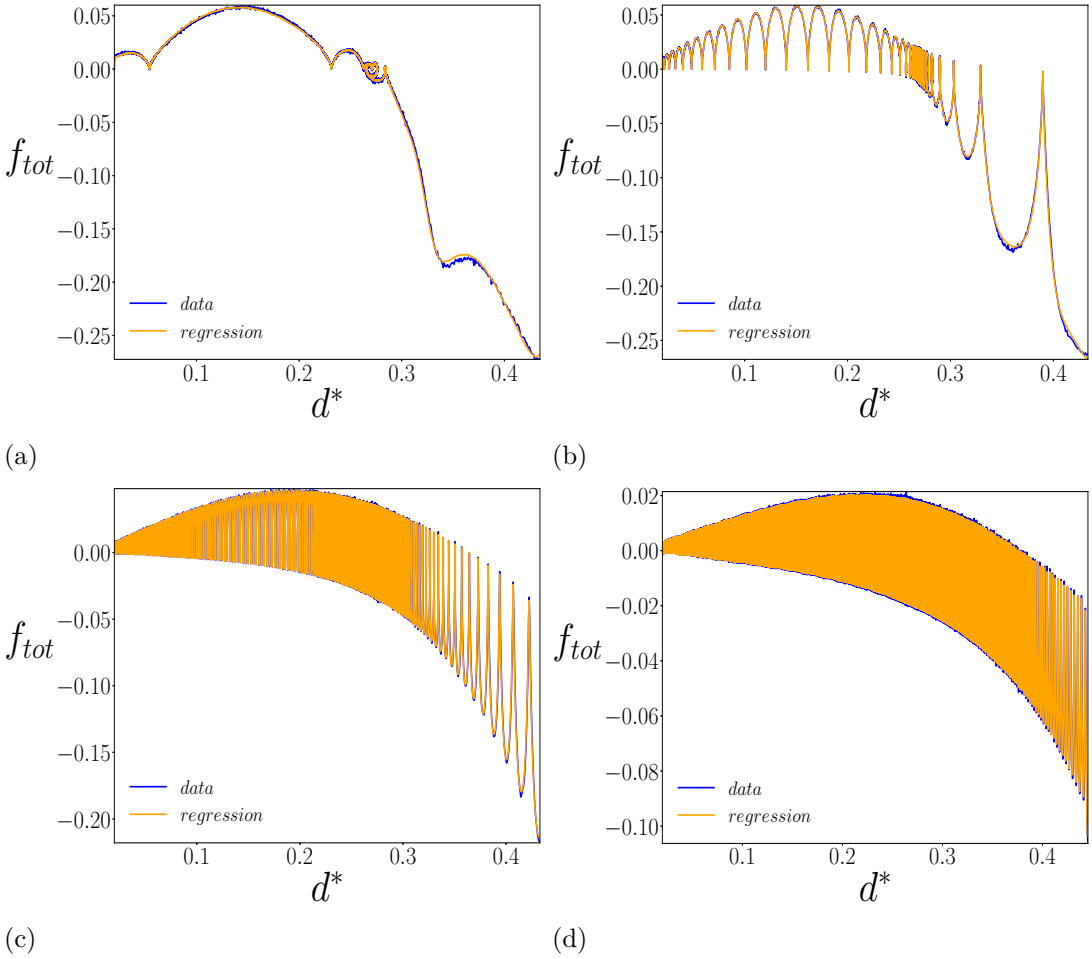

Figure 4.9. The fitted total lift coefficients to the ground-truth data using the introduced non-linear regression at $Ca = 1.67$ and (a) $\omega^* = 0.01$, (b) $\omega^* = 0.1$, (c) $\omega^* = 0.5$, and (d) $\omega^* = 1$

5. CONCLUSIONS

We investigated the dynamics of deformable capsules and droplets in steady, oscillatory, and pulsating microchannel flows of Newtonian fluid and unraveled the effects of deformability, inertia, size, and oscillation frequency on the particle motion. Our results showed that the equilibrium positions of capsules and droplets in oscillatory flows are different from those in steady flows having the same particle deformability and channel flow rate. We further observed that the pulsating flow adds even more new particle focal points as well as increases the throughput of oscillatory flows while keeping all other parameters in the system fixed. This feature of oscillatory and pulsating flows is significant because it enables a non-invasive control of the motion of the cell within microchannels, which is beneficial for numerous clinical and biological applications. Moreover, we noted that increasing the flow rate, oscillation frequency, and capsule stiffness all reduce the required length of the microchannel. In addition, the amplitude of fluctuations in the lateral trajectory of the drop, the average of the oscillatory deformation, and the average migration velocity all decrease by increasing the frequency. We also studied the lift force profiles acting on a drop having different deformabilities in steady and oscillatory flows with different frequencies. We used non-linear regression to fit the steady and oscillatory lift profiles and developed a multi-fidelity Gaussian processes model to predict the main coefficients (including the drop equilibrium point) to determine fourth-order polynomials to fit the steady and averaged oscillatory lifts with excellent accuracies. This analysis is done over a wide, continuous range of input parameters and is crucial for designing microfluidic devices for various practices.

The experimental studies on inertial microfluidic devices used for separating and focusing of cells show that such cells have various inherent characteristics, which is out of our control. The introduced oscillatory and pulsating flow regimes provide us with an extra controllable parameter to manipulate the motion of cells non-invasively. As recent progress in fabrication methods at micro and nano-scale has enabled researchers to develop microfluidic devices with complex geometries, it is then advisable to study the dynamics of such cells inside microchannels with different cross-sections. Furthermore, the rheology analysis and simulations of a suspension of cells with different properties in oscillatory flows could

reflect more realistic conditions in microfluidic systems. It is also recommended to perform a theoretical lift force analysis in oscillatory flows and provide a mathematical foundation, especially to identify the lift force equations for such flow regimes given any combination of input parameters, similar to the analysis presented in this work.

REFERENCES

[1] D. Di Carlo, D. Irimia, R. G. Tompkins, and M. Toner, "Continuous inertial focusing, ordering, and separation of particles in microchannels," *Proceedings of the National Academy of Sciences*, vol. 104, no. 48, pp. 18 892–18 897, 2007.

[2] D. R. Gossett, W. M. Weaver, A. J. Mach, S. C. Hur, H. T. K. Tse, W. Lee, H. Amini, and D. Di Carlo, "Label-free cell separation and sorting in microfluidic systems," *Analytical and bioanalytical chemistry*, vol. 397, no. 8, pp. 3249–3267, 2010.

[3] M. Toner and D. Irimia, "Blood-on-a-chip," *Annu. Rev. Biomed. Eng.*, vol. 7, pp. 77–103, 2005.

[4] D. R. Gossett, H. T. K. Tse, J. S. Dudani, K. Goda, T. A. Woods, S. W. Graves, and D. Di Carlo, "Inertial manipulation and transfer of microparticles across laminar fluid streams," *Small*, vol. 8, no. 17, pp. 2757–2764, 2012.

[5] A. Karimi, S. Yazdi, and A. Ardekani, "Hydrodynamic mechanisms of cell and particle trapping in microfluidics," *Biomicrofluidics*, vol. 7, no. 2, p. 021 501, 2013.

[6] A. van de Stolpe, K. Pantel, S. Sleijfer, L. W. Terstappen, and J. M. Den Toonder, *Circulating tumor cell isolation and diagnostics: Toward routine clinical use*, 2011.

[7] E. Sollier, D. E. Go, J. Che, D. R. Gossett, S. O'Byrne, W. M. Weaver, N. Kummer, M. Rettig, J. Goldman, N. Nickols, *et al.*, "Size-selective collection of circulating tumor cells using vortex technology," *Lab on a Chip*, vol. 14, no. 1, pp. 63–77, 2014.

[8] K. Krabchi, F. Gros-Louis, J. Yan, M. Bronsard, J. Masse, J.-C. Forest, and R. Drouin, "Quantification of all fetal nucleated cells in maternal blood between the 18th and 22nd weeks of pregnancy using molecular cytogenetic techniques," *Clinical genetics*, vol. 60, no. 2, pp. 145–150, 2001.

[9] D. Di Carlo, J. F. Edd, D. Irimia, R. G. Tompkins, and M. Toner, "Equilibrium separation and filtration of particles using differential inertial focusing," *Analytical chemistry*, vol. 80, no. 6, pp. 2204–2211, 2008.

[10] W. C. Lee, A. A. S. Bhagat, S. Huang, K. J. Van Vliet, J. Han, and C. T. Lim, "High-throughput cell cycle synchronization using inertial forces in spiral microchannels," *Lab on a Chip*, vol. 11, no. 7, pp. 1359–1367, 2011.

[11] M. E. Warkiani, B. L. Khoo, L. Wu, A. K. P. Tay, A. A. S. Bhagat, J. Han, and C. T. Lim, "Ultra-fast, label-free isolation of circulating tumor cells from blood using spiral microfluidics," *Nature protocols*, vol. 11, no. 1, p. 134, 2016.

[12] P. Sethu, A. Sin, and M. Toner, "Microfluidic diffusive filter for apheresis (leukapheresis)," *Lab on a Chip*, vol. 6, no. 1, pp. 83–89, 2006.

[13] D. R. Gossett, T. Henry, S. A. Lee, Y. Ying, A. G. Lindgren, O. O. Yang, J. Rao, A. T. Clark, and D. Di Carlo, "Hydrodynamic stretching of single cells for large population mechanical phenotyping," *Proceedings of the National Academy of Sciences*, vol. 109, no. 20, pp. 7630–7635, 2012.

[14] E. Ozkumur, A. M. Shah, J. C. Ciciliano, B. L. Emmink, D. T. Miyamoto, E. Brachtel, M. Yu, P.-i. Chen, B. Morgan, J. Trautwein, *et al.*, "Inertial focusing for tumor antigen–dependent and–independent sorting of rare circulating tumor cells," *Science translational medicine*, vol. 5, no. 179, 179ra47–179ra47, 2013.

[15] J. M. Martel, K. C. Smith, M. Dlamini, K. Pletcher, J. Yang, M. Karabacak, D. A. Haber, R. Kapur, and M. Toner, "Continuous flow microfluidic bioparticle concentrator," *Scientific reports*, vol. 5, p. 11 300, 2015.

[16] B. Miller, M. Jimenez, and H. Bridle, "Cascading and parallelising curvilinear inertial focusing systems for high volume, wide size distribution, separation and concentration of particles," *Scientific reports*, vol. 6, p. 36 386, 2016.

[17] S. C. Hur, H. T. K. Tse, and D. Di Carlo, "Sheathless inertial cell ordering for extreme throughput flow cytometry," *Lab on a Chip*, vol. 10, no. 3, pp. 274–280, 2010.

[18] B. R. Mutlu, K. C. Smith, J. F. Edd, P. Nadar, M. Dlamini, R. Kapur, and M. Toner, "Non-equilibrium inertial separation array for high-throughput, large-volume blood fractionation," *Scientific Reports*, vol. 7, no. 1, p. 9915, 2017.

[19] P. Gascoyne, J. Satayavivad, and M. Ruchirawat, "Microfluidic approaches to malaria detection," *Acta tropica*, vol. 89, no. 3, pp. 357–369, 2004.

[20] M. D. Vahey and J. Voldman, "An equilibrium method for continuous-flow cell sorting using dielectrophoresis," *Analytical chemistry*, vol. 80, no. 9, pp. 3135–3143, 2008.

[21] S. Miltenyi, W. Müller, W. Weichel, and A. Radbruch, "High gradient magnetic cell separation with macs," *Cytometry: The Journal of the International Society for Analytical Cytology*, vol. 11, no. 2, pp. 231–238, 1990.

[22] S. Zheng, H. Lin, J.-Q. Liu, M. Balic, R. Datar, R. J. Cote, and Y.-C. Tai, "Membrane microfilter device for selective capture, electrolysis and genomic analysis of human circulating tumor cells," *Journal of chromatography A*, vol. 1162, no. 2, pp. 154–161, 2007.

[23] B. R. Mutlu, J. F. Edd, and M. Toner, "Oscillatory inertial focusing in infinite microchannels," *Proceedings of the National Academy of Sciences*, vol. 115, no. 30, pp. 7682–7687, 2018.

[24] D. Di Carlo, "Inertial microfluidics," *Lab on a Chip*, vol. 9, no. 21, pp. 3038–3046, 2009.

[25] J. Skog, T. Würdinger, S. Van Rijn, D. H. Meijer, L. Gainche, W. T. Curry Jr, B. S. Carter, A. M. Krichevsky, and X. O. Breakefield, "Glioblastoma microvesicles transport rna and proteins that promote tumour growth and provide diagnostic biomarkers," *Nature cell biology*, vol. 10, no. 12, p. 1470, 2008.

[26] S. A. Melo, L. B. Luecke, C. Kahlert, A. F. Fernandez, S. T. Gammon, J. Kaye, V. S. LeBleu, E. A. Mittendorf, J. Weitz, N. Rahbari, *et al.*, "Glypican-1 identifies cancer exosomes and detects early pancreatic cancer," *Nature*, vol. 523, no. 7559, p. 177, 2015.

[27] A. J. Mach and D. Di Carlo, "Continuous scalable blood filtration device using inertial microfluidics," *Biotechnology and bioengineering*, vol. 107, no. 2, pp. 302–311, 2010.

[28] M. E. Warkiani, A. K. P. Tay, B. L. Khoo, X. Xiaofeng, J. Han, and C. T. Lim, "Malaria detection using inertial microfluidics," *Lab on a Chip*, vol. 15, no. 4, pp. 1101–1109, 2015.

[29] J. Takagi, M. Yamada, M. Yasuda, and M. Seki, "Continuous particle separation in a microchannel having asymmetrically arranged multiple branches," *Lab on a Chip*, vol. 5, no. 7, pp. 778–784, 2005.

[30] D. Matsunaga, Y. Imai, T. Yamaguchi, and T. Ishikawa, "Deformation of a spherical capsule under oscillating shear flow," *Journal of Fluid Mechanics*, vol. 762, pp. 288–301, 2015.

[31] S. H. Bryngelson and J. B. Freund, "Non-modal floquet stability of capsules in large-amplitude oscillatory extensional flow," *European Journal of Mechanics-B/Fluids*, vol. 77, pp. 171–176, 2019.

[32] C. Dietsche, B. R. Mutlu, J. F. Edd, P. Koumoutsakos, and M. Toner, "Dynamic particle ordering in oscillatory inertial microfluidics," *Microfluidics and Nanofluidics*, vol. 23, no. 6, p. 83, 2019.

[33] K. Chaudhury, S. Mandal, and S. Chakraborty, "Droplet migration characteristics in confined oscillatory microflows," *Physical Review E*, vol. 93, no. 2, p. 023 106, 2016.

[34] S. Pawowska, P. Nakielski, F. Pierini, I. K. Piechocka, K. Zembrzycki, and T. A. Kowalewski, "Lateral migration of electrospun hydrogel nanofilaments in an oscillatory flow," *PloS one*, vol. 12, no. 11, 2017.

[35] S. Pawowska, "Diffusion and migration of nano particles and filaments suspended in oscillating flow," *IPPT Reports on Fundamental Technological Research*, no. 2, pp. 1–106, 2018.

[36] K. Sarkar and W. R. Schowalter, "Deformation of a two-dimensional viscoelastic drop at non-zero reynolds number in time-periodic extensional flows," *Journal of non-newtonian fluid mechanics*, vol. 95, no. 2-3, pp. 315–342, 2000.

[37] Y. Zhang, Y. Han, L. Zhang, Q. Chen, M. Ding, and T. Shi, "Dynamic mode of viscoelastic capsules in steady and oscillating shear flow," *Physics of Fluids*, vol. 32, no. 10, p. 103 310, 2020.

[38] Z. Lu, E. D. Dupuis, V. K. Patel, A. M. Momen, and S. Shahab, "Ultrasonic oscillatory two-phase flow in microchannels," *Physics of Fluids*, vol. 33, no. 3, p. 032 003, 2021.

[39] P. G. Erlandsson and N. D. Robinson, "Electrolysis-reducing electrodes for electrokinetic devices," *Electrophoresis*, vol. 32, no. 6-7, pp. 784–790, 2011.

[40] P. Perdikaris, M. Raissi, A. Damianou, N. Lawrence, and G. E. Karniadakis, "Nonlinear information fusion algorithms for data-efficient multi-fidelity modelling," *Proceedings of the Royal Society A: Mathematical, Physical and Engineering Sciences*, vol. 473, no. 2198, p. 20 160 751, 2017.

[41] H. Babaee, P. Perdikaris, C. Chryssostomidis, and G. Karniadakis, "Multi-fidelity modelling of mixed convection based on experimental correlations and numerical simulations," *Journal of Fluid Mechanics*, vol. 809, pp. 895–917, 2016.

[42] J. M. Martel and M. Toner, "Inertial focusing in microfluidics," *Annual review of biomedical engineering*, vol. 16, pp. 371–396, 2014.

[43] S. R. Bazaz, A. Mashhadian, A. Ehsani, S. C. Saha, T. Krüger, and M. E. Warkiani, "Computational inertial microfluidics: A review," *Lab on a Chip*, vol. 20, no. 6, pp. 1023–1048, 2020.

[44] S. Connolly, D. Newport, and K. McGourty, "The mechanical responses of advecting cells in confined flow," *Biomicrofluidics*, vol. 14, no. 3, p. 031 501, 2020.

[45] D. Stoecklein and D. Di Carlo, "Nonlinear microfluidics," *Analytical chemistry*, vol. 91, no. 1, pp. 296–314, 2018.

[46] D. Di Carlo, J. F. Edd, K. J. Humphry, H. A. Stone, and M. Toner, "Particle segregation and dynamics in confined flows," *Physical review letters*, vol. 102, no. 9, p. 094 503, 2009.

[47] C. Prohm and H. Stark, "Feedback control of inertial microfluidics using axial control forces," *Lab on a Chip*, vol. 14, no. 12, pp. 2115–2123, 2014.

[48] J. Su, X. Chen, Y. Zhu, and G. Hu, "Machine learning assisted fast prediction of inertial lift in microchannels," *Lab on a Chip*, 2021.

[49] Q. Wang, D. Yuan, and W. Li, "Analysis of hydrodynamic mechanism on particles focusing in micro-channel flows," *Micromachines*, vol. 8, no. 7, p. 197, 2017.

[50] E. S. Asmolov, A. L. Dubov, T. V. Nizkaya, J. Harting, and O. I. Vinogradova, "Inertial focusing of finite-size particles in microchannels," *Journal of Fluid Mechanics*, vol. 840, pp. 613–630, 2018.

[51] C. Liu, C. Xue, J. Sun, and G. Hu, "A generalized formula for inertial lift on a sphere in microchannels," *Lab on a Chip*, vol. 16, no. 5, pp. 884–892, 2016.

[52] M. Zastawny, G. Mallouppas, F. Zhao, and B. Van Wachem, "Derivation of drag and lift force and torque coefficients for non-spherical particles in flows," *International Journal of Multiphase Flow*, vol. 39, pp. 227–239, 2012.

[53] F. O. Mannan and K. Leiderman, "Weak inertial effects on arbitrarily shaped objects in the presence of a wall," *Physical Review Fluids*, vol. 5, no. 4, p. 044 102, 2020.

[54] X. Chen, C. Xue, L. Zhang, G. Hu, X. Jiang, and J. Sun, "Inertial migration of deformable droplets in a microchannel," *Physics of Fluids*, vol. 26, no. 11, p. 112 003, 2014.

[55] J. Rivero-Rodriguez and B. Scheid, "Bubble dynamics in microchannels: Inertial and capillary migration forces–corrigendum," *Journal of Fluid Mechanics*, vol. 855, pp. 1242–1245, 2018.

[56] C. A. Stan, L. Guglielmini, A. K. Ellerbee, D. Caviezel, H. A. Stone, and G. M. Whitesides, "Sheathless hydrodynamic positioning of buoyant drops and bubbles inside microchannels," *Physical Review E*, vol. 84, no. 3, p. 036 302, 2011.

[57] J. Zhou and I. Papautsky, "Fundamentals of inertial focusing in microchannels," *Lab on a Chip*, vol. 13, no. 6, pp. 1121–1132, 2013.

[58] A. H. Raffiee, A. M. Ardekani, and S. Dabiri, "Numerical investigation of elasto-inertial particle focusing patterns in viscoelastic microfluidic devices," *Journal of Non-Newtonian Fluid Mechanics*, vol. 272, p. 104 166, 2019.

[59] C. Schaaf and H. Stark, "Inertial migration and axial control of deformable capsules," *Soft Matter*, vol. 13, no. 19, pp. 3544–3555, 2017.

[60] S. O. Unverdi and G. Tryggvason, "A front-tracking method for viscous, incompressible, multi-fluid flows," *Journal of computational physics*, vol. 100, no. 1, pp. 25–37, 1992.

[61] R. Skalak, A. Tozeren, R. Zarda, and S. Chien, "Strain energy function of red blood cell membranes," *Biophysical journal*, vol. 13, no. 3, p. 245, 1973.

[62] T. Krüger, B. Kaoui, and J. Harting, "Interplay of inertia and deformability on rheological properties of a suspension of capsules," *Journal of Fluid Mechanics*, vol. 751, pp. 725–745, 2014.

[63] K. Parker and C. Winlove, "The deformation of spherical vesicles with permeable, constant-area membranes: Application to the red blood cell," *Biophysical journal*, vol. 77, no. 6, pp. 3096–3107, 1999.

[64] J. Charrier, S. Shrivastava, and R. Wu, "Free and constrained inflation of elastic membranes in relation to thermoformingnon-axisymmetric problems," *The Journal of Strain Analysis for Engineering Design*, vol. 24, no. 2, pp. 55–74, 1989.

[65] A. H. Raffiee, S. Dabiri, and A. M. Ardekani, "Deformation and buckling of microcapsules in a viscoelastic matrix," *Physical Review E*, vol. 96, no. 3, p. 032 603, 2017.

[66] S. J. Shin and H. J. Sung, "Dynamics of an elastic capsule in moderate reynolds number poiseuille flow," *International journal of heat and fluid flow*, vol. 36, pp. 167–177, 2012.

[67] B. Kim, C. B. Chang, S. G. Park, and H. J. Sung, "Inertial migration of a 3d elastic capsule in a plane poiseuille flow," *International Journal of Heat and Fluid Flow*, vol. 54, pp. 87–96, 2015.

[68] H. Lan, S. C. Hur, D. Di Carlo, and D. B. Khismatullin, "Lateral migration of living cells in inertial microfluidic systems explored by fully three-dimensional numerical simulation," *arXiv preprint arXiv:1306.4709*, 2013.

[69] M. M. Villone, "Lateral migration of deformable particles in microfluidic channel flow of newtonian and viscoelastic media: A computational study," *Microfluidics and Nanofluidics*, vol. 23, no. 3, p. 47, 2019.

[70] B. Dincau, E. Dressaire, and A. Sauret, "Pulsatile flow in microfluidic systems," *Small*, vol. 16, no. 9, p. 1 904 032, 2020.

[71] M. E. Fay, D. R. Myers, A. Kumar, C. T. Turbyfield, R. Byler, K. Crawford, R. G. Mannino, A. Laohapant, E. A. Tyburski, Y. Sakurai, *et al.*, "Cellular softening mediates leukocyte demargination and trafficking, thereby increasing clinical blood counts," *Proceedings of the National Academy of Sciences*, vol. 113, no. 8, pp. 1987–1992, 2016.

[72] J. Zhang, S. Yan, D. Yuan, G. Alici, N.-T. Nguyen, M. E. Warkiani, and W. Li, "Fundamentals and applications of inertial microfluidics: A review," *Lab on a Chip*, vol. 16, no. 1, pp. 10–34, 2016.

[73] P.-H. Chan and L. Leal, "The motion of a deformable drop in a second-order fluid," *Journal of Fluid Mechanics*, vol. 92, no. 1, pp. 131–170, 1979.

[74] C. A. Stan, A. K. Ellerbee, L. Guglielmini, H. A. Stone, and G. M. Whitesides, "The magnitude of lift forces acting on drops and bubbles in liquids flowing inside microchannels," *Lab on a Chip*, vol. 13, no. 3, pp. 365–376, 2013.

[75] G. Vishwanathan and G. Juarez, "Generation and application of sub-kilohertz oscillatory flows in microchannels," *Microfluidics and Nanofluidics*, vol. 24, no. 9, pp. 1–10, 2020.

[76] G. Segre and A. Silberberg, "Radial particle displacements in poiseuille flow of suspensions," *Nature*, vol. 189, no. 4760, pp. 209–210, 1961.

[77] A. H. Raffiee, S. Dabiri, and A. M. Ardekani, "Elasto-inertial migration of deformable capsules in a microchannel," *Biomicrofluidics*, vol. 11, no. 6, p. 064 113, 2017.

[78] A. Kilimnik, W. Mao, and A. Alexeev, "Inertial migration of deformable capsules in channel flow," *Physics of fluids*, vol. 23, no. 12, p. 123 302, 2011.

[79] H. Noguchi, "Dynamic modes of red blood cells in oscillatory shear flow," *Physical Review E*, vol. 81, no. 6, p. 061 920, 2010.

[80] C. Song, S. J. Shin, H. J. Sung, and K.-S. Chang, "Dynamic fluid–structure interaction of an elastic capsule in a viscous shear flow at moderate reynolds number," *Journal of fluids and structures*, vol. 27, no. 3, pp. 438–455, 2011.

[81] A. Diaz, N. Pelekasis, and D. Barthes-Biesel, "Transient response of a capsule subjected to varying flow conditions: Effect of internal fluid viscosity and membrane elasticity," *Physics of Fluids*, vol. 12, no. 5, pp. 948–957, 2000.

[82] L. Zhu, J. Rabault, and L. Brandt, "The dynamics of a capsule in a wall-bounded oscillating shear flow," *Physics of Fluids*, vol. 27, no. 7, p. 071 902, 2015.

[83] M. Zhao and P. Bagchi, "Dynamics of microcapsules in oscillating shear flow," *Physics of Fluids*, vol. 23, no. 11, p. 111 901, 2011.

[84] S. Dabiri and P. Bhuvankar, "Scaling law for bubbles rising near vertical walls," *Physics of Fluids*, vol. 28, no. 6, p. 062 101, 2016.

[85] M. Bayareh, A. Doostmohammadi, S. Dabiri, and A. Ardekani, "On the rising motion of a drop in stratified fluids," *Physics of Fluids*, vol. 25, no. 10, p. 023 029, 2013.

[86] X. Chen, J. Lu, and G. Tryggvason, "Numerical simulation of self-propelled non-equal sized droplets," *Physics of Fluids*, vol. 31, no. 5, p. 052 107, 2019.

[87] W. Li, J. Lu, G. Tryggvason, and Y. Zhang, "Numerical study of droplet motion on discontinuous wetting gradient surface with rough strip," *Physics of Fluids*, vol. 33, no. 1, p. 012 111, 2021.

[88] H. Xu and B. F. Bai, "Unsynchronized motion of inner and outer membranes of compound capsules in shear flow," *Physics of Fluids*, vol. 32, no. 12, p. 127 115, 2020.

[89] Z. Y. Luo, X. L. Shang, and B. F. Bai, "Effect of soluble surfactant on the motion of a confined droplet in a square microchannel," *Physics of Fluids*, vol. 31, no. 11, p. 117 104, 2019.

[90] E. J. Campbell and P. Bagchi, "A computational model of amoeboid cell swimming," *Physics of Fluids*, vol. 29, no. 10, p. 101 902, 2017.

[91] D.-y. Pan, Y.-q. Lin, L.-x. Zhang, and X.-m. Shao, "Motion and deformation of immiscible droplet in plane poiseuille flow at low reynolds number," *Journal of Hydrodynamics*, vol. 28, no. 4, pp. 702–708, 2016.

[92] H. Lan and D. B. Khismatullin, "A numerical study of the lateral migration and deformation of drops and leukocytes in a rectangular microchannel," *International journal of multiphase flow*, vol. 47, pp. 73–84, 2012.

[93] M. Razi and M. Pourghasemi, "Direct numerical simulation of deformable droplets motion with uncertain physical properties in macro and micro channels," *Computers & Fluids*, vol. 154, pp. 200–210, 2017.

[94] M. C. Kennedy and A. O'Hagan, "Predicting the output from a complex computer code when fast approximations are available," *Biometrika*, vol. 87, no. 1, pp. 1–13, 2000.

[95] L. Le Gratiet and J. Garnier, "Recursive co-kriging model for design of computer experiments with multiple levels of fidelity," *International Journal for Uncertainty Quantification*, vol. 4, no. 5, 2014.

[96] B. Ho and L. Leal, "Inertial migration of rigid spheres in two-dimensional unidirectional flows," *Journal of fluid mechanics*, vol. 65, no. 2, pp. 365–400, 1974.

[97] P. Bagchi and S. Balachandar, "Shear versus vortex-induced lift force on a rigid sphere at moderate re," *Journal of Fluid Mechanics*, vol. 473, pp. 379–388, 2002.

[98] N. Aggarwal and K. Sarkar, "Deformation and breakup of a viscoelastic drop in a newtonian matrix under steady shear," *Journal of Fluid Mechanics*, vol. 584, pp. 1–21, 2007.

[99] R. L. Marson, Y. Huang, M. Huang, T. Fu, and R. G. Larson, "Inertio-capillary cross-streamline drift of droplets in poiseuille flow using dissipative particle dynamics simulations," *Soft matter*, vol. 14, no. 12, pp. 2267–2280, 2018.

[100] P. Hadikhani, S. M. H. Hashemi, G. Balestra, L. Zhu, M. A. Modestino, F. Gallaire, and D. Psaltis, "Inertial manipulation of bubbles in rectangular microfluidic channels," *Lab on a Chip*, vol. 18, no. 7, pp. 1035–1046, 2018.

[101] S. Mortazavi and G. Tryggvason, "A numerical study of the motion of drops in poiseuille flow. part 1. lateral migration of one drop," *Journal of Fluid Mechanics*, vol. 411, pp. 325–350, 2000.

[102] A. Lafzi, A. H. Raffiee, and S. Dabiri, "Inertial migration of a deformable capsule in an oscillatory flow in a microchannel," *Physical Review E*, vol. 102, no. 6, p. 063 110, 2020.

[103] V. O'Brien, "Pulsatile fully developed flow in rectangular channels," *Journal of the Franklin Institute*, vol. 300, no. 3, pp. 225–230, 1975.

[104] M. Karbaschi, A. Javadi, D. Bastani, and R. Miller, "High frequency oscillatory flow in micro channels," *Colloids and Surfaces A: Physicochemical and Engineering Aspects*, vol. 460, pp. 355–360, 2014.

[105] T. Inamuro, R. Tomita, and F. Ogino, "Lattice boltzmann simulations of drop deformation and breakup in shear flows," *International Journal of Modern Physics B*, vol. 17, no. 01n02, pp. 21–26, 2003.

[106] D. Alghalibi, M. E. Rosti, and L. Brandt, "Inertial migration of a deformable particle in pipe flow," *Physical Review Fluids*, vol. 4, no. 10, p. 104 201, 2019.

[107] A. Lafzi and S. Dabiri, "Dynamics of droplet migration in oscillatory and pulsating microchannel flows and prediction and uncertainty quantification of its lateral equilibrium position using multifidelity gaussian processes," *Physics of Fluids*, vol. 33, no. 6, p. 062 010, 2021.

[108] K. W. Seo, Y. J. Kang, and S. J. Lee, "Lateral migration and focusing of microspheres in a microchannel flow of viscoelastic fluids," *Physics of Fluids*, vol. 26, no. 6, p. 063 301, 2014.

[109] M. Ishii and N. Zuber, "Drag coefficient and relative velocity in bubbly, droplet or particulate flows," *AIChE journal*, vol. 25, no. 5, pp. 843–855, 1979.

[110] M. R. Snyder, O. M. Knio, J. Katz, and O. P. Le Matre, "Statistical analysis of small bubble dynamics in isotropic turbulence," *Physics of Fluids*, vol. 19, no. 6, p. 065 108, 2007.

[111] Y. Zhou, C. Zhao, and H. Bo, "Analyses and modified models for bubble shape and drag coefficient covering a wide range of working conditions," *International Journal of Multiphase Flow*, vol. 127, p. 103 265, 2020.

[112] G. Kelbaliyev and K. Ceylan, "Development of new empirical equations for estimation of drag coefficient, shape deformation, and rising velocity of gas bubbles or liquid drops," *Chemical Engineering Communications*, vol. 194, no. 12, pp. 1623–1637, 2007.

[113] A. K. Salibindla, A. U. M. Masuk, S. Tan, and R. Ni, "Lift and drag coefficients of deformable bubbles in intense turbulence determined from bubble rise velocity," *Journal of Fluid Mechanics*, vol. 894, 2020.

[114] K. Ceylan, A. Altunba, and G. Kelbaliyev, "A new model for estimation of drag force in the flow of newtonian fluids around rigid or deformable particles," *Powder technology*, vol. 119, no. 2-3, pp. 250–256, 2001.

[115] C. Shao, K. Luo, and J. Fan, "Detailed numerical simulation of unsteady drag coefficient of deformable droplet," *Chemical Engineering Journal*, vol. 308, pp. 619–631, 2017.

[116] S. Aggarwal and F. Peng, "A review of droplet dynamics and vaporization modeling for engineering calculations," 1995.

[117] H. Sundqvist and G. Veronis, "A simple finite-difference grid with non-constant intervals," *Tellus*, vol. 22, no. 1, pp. 26–31, 1970.

[118] S. Jahromi, E. Amani, and S. Movahed, "An improved hybrid continuum-atomistic four-way coupled model for electrokinetics in nanofluidics," *Electrophoresis*, vol. 40, no. 12-13, pp. 1678–1690, 2019.

VITA

Education

PhD in Agricultural and Biological Engineering, **Purdue University**, 2018-2022

MSc in Mechanical Engineering, **University of Washington**, 2015-2017

BSc in Mechanical Engineering, **University of Tehran**, 2010-2015

Journal Publications

A. Lafzi, A.H. Raffiee, and S. Dabiri, "Inertial migration of a deformable capsule in an oscillatory flow in a microchannel." Physical Review E 102, no. 6 (2020): 063110.

A. Lafzi, and S. Dabiri, "Dynamics of droplet migration in oscillatory and pulsating microchannel flows and prediction and uncertainty quantification of its lateral equilibrium position using multifidelity Gaussian processes." Physics of Fluids 33, no. 6 (2021): 062010.

A. Lafzi, M. Boodaghi, S. Zamani, N. Mohammadshafie, and V. R. Hasti. "Analysis of the effectiveness of face-coverings on the death ratio of COVID-19 using machine learning." Scientific Reports 11, no. 1 (2021): 1-12.

Manuscripts Under Review

A. Lafzi, and S. Dabiri, "A numerical lift force analysis on the inertial migration of a deformable droplet in steady and oscillatory microchannel flows." Lab on a Chip

Conference Presentations

A. Lafzi, A.H. Raffiee, and S. Dabiri, "New insights into the migration patterns of a single capsule flowing in a pulsating microchannel." In APS Division of Fluid Dynamics Meeting Abstracts, pp. B35-004. 2019.